DELFT UNIVERSITY OF TECHNOLOGY

TUDelft Delft University of Technology

Thesis

Ultrasound Imaging Using
a Single Element Transducer

---

submitted in partial fulfillment of the
requirements for the degree of

MASTER OF SCIENCE
in
ELECTRICAL ENGINEERING
by

Andrejs Fedjajevs (4418824)

Company supervisor:

Pieter Kruizinga
Postdoctoral researcher
in
Erasmus MC

Erasmus MC
University Medical Center Rotterdam

University supervisor:

Geert Leus
Professor
in the
Department of Microelectronics

TUDelft Delft University of Technology

14th September, 2016

"Try not to stand out, try to be modest ... climbing into the limelight is bound to be one at the expense of the others who won't be climbing. That you must step on somebody's toes doesn't mean you should stand on their shoulders. "

Joseph Brodsky

Acknowledgments

Writing this part of the thesis offers me great pleasure. Not only because at this point I already can see the end of my studies, but mostly because it is an opportunity to thank all the people supporting me.

My foremost gratitude goes to my supervisor, Pieter Kruizinga, without whom this project would definitely be another story. I highly appreciate his guidance in research and numerous hours he spent, but also the atmosphere of respect and openness he was able to create in our room on the 23rd floor. If I do not stay in the medical industry, I might forget some of ultrasound concepts, but I will remember how to think positively and productively at the same time.

I would like to thank my university professor, Geert Leus, for everything he taught during the first year courses and our thesis related meetings. Prof. Leus is a recognized scientist, but also an excellent lecturer (these two not always come together).

I want to thank my friend and colleague, with whom I shared the greatest possible view of Rotterdam – Pim van der Meulen. Thank you, Pim, for the invaluable ideas you proposed and the discussions we had near the blackboard. Also, lunches and coffee-breaks would have not been complete without our talks about history, culture, languages, etc. In general, I know a lot more about the Netherlands thanks to you.

I also want to thank Frits Mastik, Robert Beurskens and Geert Springeling. I appreciate their willingness to help and broad skills in solving any issue effectively and fast. Their contribution to this project is much bigger than it might seem.

I use this opportunity to thank all members of the Biomedical Engineering Group. I had a chance to watch a PhD candidate's everyday work more closely, I have visited several scientific conferences and learned a lot from that. I always felt as being a colleague here.

Special gratitude to my family for their support, patience and confidence in my final success. Sometimes the only thing that is needed, is to hear that you are doing everything right.

Contents

List of Figures

Abbreviations

MRI	Magnetic Resonance Imaging
B	Bandwidth
f_s	sampling frequency
CT	Computer Tomography
CS	Compressive Sensing
FT	Fourier Transform
ASA	Angular Spectrum Approach
ROI	Region of Interest
SNR	Signal-to-Noise Ratio
PRF	Pulse Repetition Frequency
TMM	Tissue Mimicking Material

Motivation and Objectives

Thanks to recent technological improvements, sensitive ultrasound probes with hundreds of elements are manufactured now [1]. These probes might have various configurations and characteristics. Despite ultrasound is the cheapest and safest for a patient diagnostic method, there is a fierce competition from the side of MRI and X-ray imaging.

Current ultrasound systems visualize 3D space in 2D images. Thus a highly trained practitioner is needed to handle the probe and to interpret the data. Even though ultrasound matrix (2D) transducers are already available, they need more ADC units, wires, etc., becoming more expensive in production and data processing.

Fortunately, the need for classical uniform sampling has been already questioned by the signal processing field called *compressive sensing* (CS) [2]. According to the theory, all natural signals (images, speech) have a sparse representation or many zero coefficients. It proves that a finite sparse signal can be reconstructed from a small set of linear, non-adaptive measurements. Unlike in classical compression – first save, then compress the data, in CS both actions are done simultaneously.

CS theory application to the field of medical imaging is very recent, even though, ultrasonography is an excellent candidate. Indeed, it is a domain which possesses a number of features calling for sparse regularization:

- high dimensionality – acoustic data (e.g. pressure fields) is represented by multi-dimensional arrays and, thus, acquisition requires high throughput and storage memory;
- data correlation – due to a small distance between the array elements, they record correlated information;
- linearity – imaging can be seen as a linear inverse problem.

Inspired by revolutionary results of CS, in this project we propose a purely analog CS imaging method using a _single_ element transducer in pulse echo regime. As an alternative to generated acquisition sequences, we use an instantaneous compressive imaging mechanism – an aberration mask, which effectively changes the transducer's spatial field.

Opposite to the conventional geometry-based reconstruction, a linear model with a redundant dictionary-matrix is employed. This approach reformulates the image reconstruction task into a system of linear equations. By means of an essential calibration procedure, the dictionary is filled with spatially variant impulse responses. Rotation of the mask is considered as an additional degree of freedom in acquiring compressed measurements.

Our simple device is able to compensate multi-element probe sacrifice. The imaging load is then shifted from hardware into software (or processing domain) which is supported by constantly growing computers' capabilities (memory, GPU's). Ideas presented in this thesis could lead to a low-profile ultrasound system occupying a new niche among medical wearable devices.

Chapter 1

Introduction

1.1 Medical Ultrasonics

1.1.1 Historical Review

The idea of using sound to see into objects was proposed by scientists long before the 20th century. The piezoelectric effect (which still remains the basis of ultrasound technology) was first demonstrated by the Curie brothers in 1880 [4]. Nevertheless, only after the two world wars demonstrated advances of the pulse-echo technique (radars and sonars), scientists and practitioners started on investigating ultrasound properties and developing equipment to look into human body.

The medical ultrasound field was triggered and began to develop rapidly in early 50's. Early examples are – the first A-scan of a stomach obtained by Dr. Wild in 1949, heart motion registered with a flaw detector by prof. Hertz in 1953 and many others. Throughout the years, biomedical engineers have developed Doppler imaging to track moving objects, 2D array probes with hundreds elements, high intensity focused ultrasound

FIGURE 1.1: An A-mode "ultrasonic Locator" designed by G.Ludwig was marketed commercially for "use in Medicine and Biology" around 1950. Suggested usage already included detection of heart motion, blood vessels, kidney stones and glass particles in the body. [3]

and other breakthroughs. Even now, more than 60 years after, ultrasonic imaging remains a growing field and makes significant contribution to clinical medicine.

J. Woo *et al.* [3] give more thorough overview of the history of medical ultrasound.

Vast usage of ultrasound nowadays, when also other techniques are available (MRI, X-ray CT), can be explained by its advantages:

- Ultrasound diagnostics does not involve ionizing radiation and is safe for human tissue (unless ultimately high intensities are used);
- Incredible cost-efficiency. Pressure generation using a piezoelectric crystal is much more straightforward, than setting up a large magnetic field for an MRI scan. Additionally, ultrasound systems do not require special safety equipment (shields) and expensive supplies;
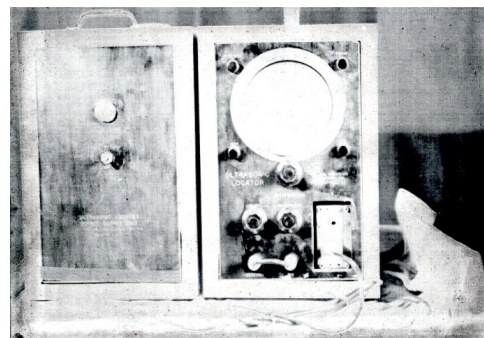
- Apart from being cheap, the ultrasound system (even the most advanced) is relatively lightweight and can be designed portable;
- Ultrasound is a dynamic technique. It presents a moving image and allows the user to change the view in real time.

1.1.2 Fundamentals of Ultrasound Imaging

In this subsection, the basic principles of ultrasound and related medical imaging systems are given. We mainly emphasize terms that have relevance for further understanding of this thesis. For more substantial explanations the reader may refer to [5, 6].

Ultrasound Interaction with Tissue

Waves can be considered as shear (transverse) or compression (longitudinal) depending on the particles' motion direction. If the motion is perpendicular to the wave itself – it is defined as a shear wave. If the particle motion is aligned with the wave – it is a compression wave.

Most of the soft tissues in human body can be properly described (in the context of ultrasound) as a fluidic material. This convention allows ignoring shear waves and makes wave modeling simpler, but still very accurate. The propagation of the wave through tissue in 3D is governed by the pressure wave equation:

$$\nabla^2 p - \frac{1}{c^2}\frac{\partial^2 p}{\partial t^2} = 0. \tag{1.1}$$

Parameter c, the speed of sound is related to the density ρ and bulk modulus K (an opposite of compressibility k) of the medium:

$$c = \sqrt{\frac{K}{\rho}}. \tag{1.2}$$

A homogeneous, non-absorbing medium would ensure that an acoustic pressure wave propagates unchanged in shape and amplitude. In reality, similar as electromagnetic waves, ultrasound waves interact with the medium in several ways. They are absorbed, scattered, or reflected by the media and inhomogeneities. When an advanced ultrasonic imaging technique is developed, these interactions must be taken into account.

Attenuation

Attenuation is a generalizing term for all mechanisms that reduce energy of an ultrasound beam. Intensity is attenuated because of three factors – power absorption, scattering losses and geometric spread.

Absorption phenomenon refers to the conversion of incident ultrasound energy into heat. It depends on medium mechanical properties and the wave frequency. The frequency dependence of the absorption coefficients of many substances empirically follows the power law $\alpha \approx \alpha_0 f^y$ [Np/cm], which in decibels is expressed as

$$\alpha_{dB} \approx 20 log_{10}(\exp^{-\alpha_0 f^y}) = 8.7\alpha_0 f^y \ [dB/cm], \tag{1.3}$$

and is often quoted as (α_{dB}/f^y) in units of dB/cm/MHz^y. Some example tissue properties are given in Table 1.1.

The wave also gets reflected and scattered, and thus attenuated. Losses induced by these processes are called *scattering losses*, however they only account for $\leq 10\%$ of the total attenuation. The least contributing factor is the so-called *geometric spread* – attenuation due to diverging regions of the beam.

Attenuation is a function of the distance traveled by the wave and its frequency. For every material the attenuation coefficient α is generally given in dB$\times$cm^{-1} per MHz. The attenuation coefficient of most tissues increases approximately linearly with frequency.

TABLE 1.1: Typical acoustic properties of tissues. [6, p.314]

tissue type	Density (g/cm^3)	Attenuation α_0 (dB/cm/MHz^{-1})	frequency dependence y	Speed of Sound (m/sec)
water (20C)	1	0.002	2	1480
blood	1.055	0.15	1.21	1575
brain	1.03	0.8	1.35	1550
liver	1.06	0.9	1.1	1590
bone	1.9	22	-	4080
muscle	1.065	3.3@1MHz	-	1575
fat	0.95	0.6	1	1450

Reflection

What happens with the beam after encountering an object (region with different mechanical properties) depend on the object's size in comparison with wavelength λ of sound.

If the obstacle is larger than λ (the process is named *specular reflection*), then part of the beam energy is reflected. The rest of the beam's energy is transmitted and continues its way as a beam of lower intensity. Exact ratios of incident, reflected and transmitted waves' amplitudes are dependent on the angle and corresponding material properties – impedances [5].

The acoustic impedance Z (in units of rayls) is the product of the medium density and ultrasound speed:

$$Z = \rho c. \tag{1.4}$$

For the special case when the wave is perpendicular to the boundary between two materials with impedances Z_1 and Z_2, the amplitude reflection coefficient is:

$$R = \frac{Z_2 - Z_1}{Z_2 + Z_1}. \tag{1.5}$$

If the object size is comparable to the wavelength λ, such inhomogeneity behaves as a point source. Energy is scattered (*scattering* or *non-specular reflection*) in many directions in the form of a spherical wave. Hence, scattering is strongly wavelength- and shape-dependent [7].

In reality, ultrasound waves encounter many obstacles that are very closely positioned. If each of them behaves as a point source and emits a spherical coherent (having the same frequency and constant phase difference) wave, one can observe the *interference* effect. This results in the *speckle* pattern which is typical for ultrasound images (Figure 1.3b). Speckle does not correspond to a real object. It is the result of constructive and destructive wave summation. It is important to emphasize that speckle is not a random process as thermal noise effects. Therefore, domain experts might be able to differentiate tissues based on speckle texture.

Sonographic Equipment

The device that converts electric signals to acoustic waves (and vice-versa) is called the *ultrasound transducer*. Numerous types of them are available – providing a wide choice of possible applications. The most important parameters for characterizing an ultrasonic transducer are:

Central frequency f_0 – is usually in the range of 1-20 MHz for medical applications. Choice of f_0 marks a trade-off between spatial resolution and penetration depth. High-frequency waves suffer more from attenuation. This provides reduced penetration, but a greater sensitivity to small discontinuities.

Focal depth – the distance from the face of the transducer to the location where ultrasound intensity is the highest. Reflectors at this distance can be imaged with the best possible quality. The transducer can be focused by design (fixed focus), using refracting lenses, or electronically (adjustable focus).

Directivity pattern – transducer's (physical) design parameter that specifies the gain applied to a signal coming from a certain direction when the transducer operates in receive mode. This parameter is a function of angle-of-arrival and frequency.

Near-field (Fresnel zone) length – region in which the beam maintains relatively constant diameter determined by the diameter of the transducer and the wave frequency.

Single element transducers were earlier used for mechanical scanning of 2D planes, but nowadays – for basic measurements, material characterization or catheter applications (intravascular ultrasound). Since the 1980's, transducer arrays (typically 16 - 192 piezo-elements) were routinely used for imaging. These are mainly divided by shapes into linear, convex and phased probes (not mentioning planar 2D-arrays). Probe type defines an area which is swept by the beam (Figure 1.2a).

Linear arrays emit parallel beams and give a rectangular view. Convex (curved) probes allow maximum field of view and better resolution due to larger aperture. Phased transducers are similar to linear, except that the beam is steered by phasing (electronically). As a result, probe dimensions are smaller at the expense of additional electronic circuitry. [8, p.27]

Echo Measurement and Beamforming

In general, the imaging process can be described as follows. The transducer is placed in contact with the tissue and an acoustic pressure wave, with center frequency f_0, is emitted. While propagating through the medium, there are several types of interactions occurring – reflection/scattering, absorption/attenuation, refraction. Some of these interactions are necessary to form an ultrasound image, whereas others produce artifacts or reduce propagating beam energy.

The ultrasonic wave is reflected from acoustic heterogeneities (differences in acoustic impedance) and an echo signal is detected by the transducer after a certain time delay. The depth at which the reflection takes place can be estimated assuming constant wave speed in the medium. The simplest one-element case is illustrated in Figure 1.3a. Array processing algorithms that are used to create uniform, narrow beam stretching in particular direction, are known under the common term - *beamformers.*

The operation is two-fold and symmetrical at emission and reception.

Firstly, transmit time delays and amplitude weights are generated and array elements are fired accordingly. Time delays are calculated so that sound waves from all transmitters will arrive at the focal point simultaneously. Afterwards, piezo-electric elements become sensors to record reflected waves.
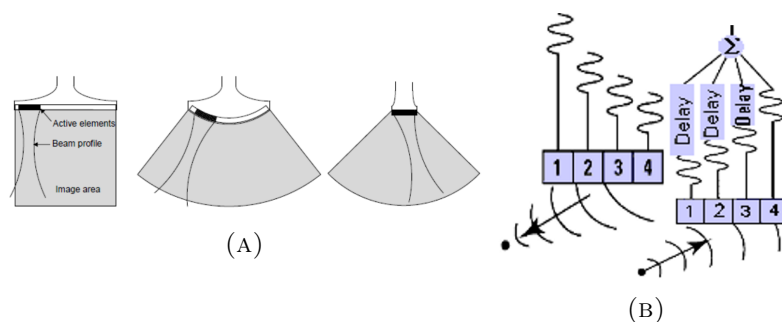
FIGURE 1.2: (A) From left to right: linear, curved and phased array transducers. [9] (B) Left pane: beam is focused and steered to the left to reach the focal point simultaneously. Right pane: the returning echo encounters element 1 before others. Signals have to be delayed to compensate for this. Then the signals are summed for subsequent processing.

The reception operation is essentially the inverse of transmit. Received signals are amplified and time-delayed by identical values. Finally, the echoes are fed to an adder. When the beam is steered towards the source, the maximum output power is registered by the system (Figure 1.2b).

By adjusting delays, the beam can be steered to every point in a scanning plane. Nowadays, focusing and steering is done digitally, and algorithms with many modifications are available – apodization can be calculated adaptively or just once (data-independently), elements fired and/or summed group-wise, etc. [10–12]

Imaging Modes

The simplest and oldest of imaging modes is the Amplitude mode (*A-mode*). It consists of a single transducer beam linearly scanning through tissue. The echo amplitudes (y-axis) are displayed as a function of time (x-axis). The time axis can be converted to depth if the speed of sound c_0 is known. A-mode is a 1D image and only "obstacles" in the direction of the beam are visible (Figure 1.3a).
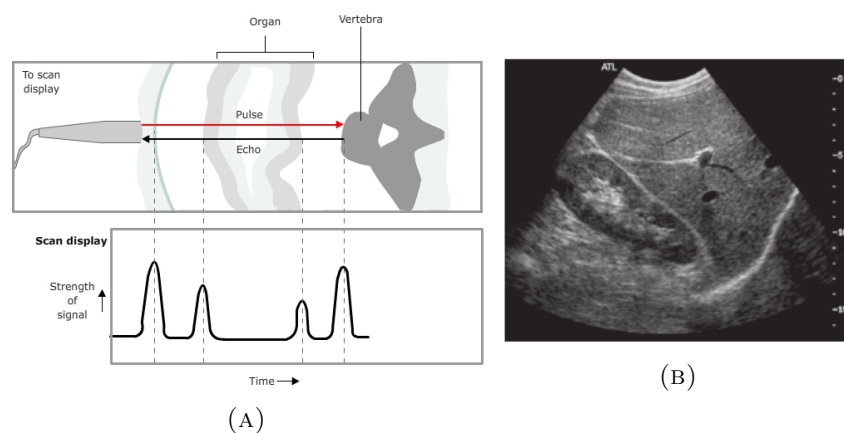
FIGURE 1.3: (A) In the A-mode echoes returning from the body are displayed as signals on an oscilloscope. [13]. (B) An example of a B-mode image showing reflections from organ and blood vessel boundaries and scattering from tissues.

Nowadays, A-mode ultrasonography is not in use anymore, being replaced by the *brightness-mode* imaging. In the B-mode, many A-scans are performed, using different beam paths, so that a plane is scanned at once. Under this mode the locations of the echo-producing interfaces are displayed in two dimensions, but the amplitude of each echo is diversified by the brightness of the corresponding pixel (Figure 1.3b).

The acquisition process is quite fast and generally allows a frame-rate of 20 to 30 images per second, which is enough for real-time realistic motion recording. B-mode is the most widespread mode in clinical routine at the moment.

There are more modes available, for example, C-mode, M-mode, Doppler-mode, Harmonic mode and others.

Image Quality

If an isolated point target in a homogeneous medium is scanned, the produced image shows a map of "smeared information" due to imperfections in reconstruction. Such a map is called the *point spread function* (PSF) or the impulse response of the *imaging system* (Figure 1.4, top row). An image of any object then can be obtained by convolving the PSF with the object field.

One of the image quality factors is the *spatial resolution* – the minimum distance separating two point-objects, which are displayed in the image as two disjoint points (or regions). Referring to an ultrasound system, the spatial resolution is represented by two numbers – *axial* and *lateral* resolutions. The PSF projection on the beam propagation axis defines the *axial resolution* (1.4, the bottom row). The PSF profile over the transducer aperture axis provides information about the *lateral* resolution (1.4, the middle row).

Both axial and lateral resolutions are governed by f_0 – the first one is dependent on the transmitted pulse length and the latter – on the beam width in the medium. This is why contemporary systems tend to employ high frequency transducers. By increasing the aperture of the transducer, smaller PSFs can be obtained. Other influencing factors are the excitation pulse length (shorter pulse leads to smaller PSF), the distance between transducer elements. For typical transducers, with frequency range up to 15 MHz, lateral resolution of 0.3-1 mm is achieved, however sub-wavelength resolution systems are also available.

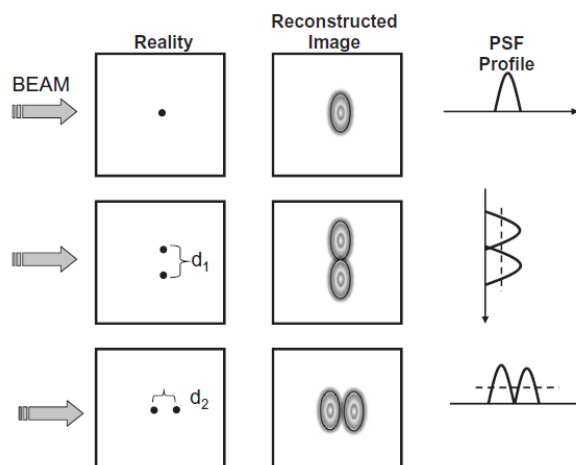FIGURE 1.4: Top row: a point target is scanned by an acoustic beam, corresponding image (center) and the axial profile (right) are shown. Middle row: two points at the distance d_1 are imaged and the lateral resolution is evaluated. Bottom row: axial resolution evaluation. [6, p.196]

Other performance measures, which are not discussed here are contrast, temporal resolution, sensitivity, etc. For further details see [5].

1.2 Examples of Compressive Sensing Projects

One of the best known statements of information theory is the Shannon-Nyquist sampling theorem, which imposes a sampling frequency f_s limit for a signal's perfect reconstruction. It states that if a signal has bandwidth B > 0, it should be sampled at the *Nyquist rate*, namely, $2B$ [14] . If $f_s < 2B$ is used, aliasing effect will affect the reconstructed data.

Unfortunately, despite nowadays computational power advances and Moore's law, often in contemporary applications the Nyquist rate is an unresolvable challenge. Not always it is a computational problem, but also a matter of practical or safety reasons.

With a hundred-element transducer of large aperture one can apply multiple transmit/receive patterns, channel coding, focusing, etc. Once we restrict ourselves to the use of a single element ultrasound device, it becomes clear, that the whole paradigm of imaging should be changed as well.

The references below exemplify, how more information can be retrieved from less sensors by taking measurements y_m in a linearly-mixed mode. They introduce a quite recent technique known as *compressive sensing* (CS) that has already shown large potential in reducing the sampling rate for such tasks as compression, MRI, facial recognition, photography, etc.

1.2.1 Single Pixel Imaging

R.Baraniuk *et.al* from the Rice University assert that CS ideas can change conventional digital photography [15]. According to them, the main inefficiency of mega-pixel cameras is that they sample images with millions of pixels, when afterwards the data has to be compressed by throwing away redundant information.
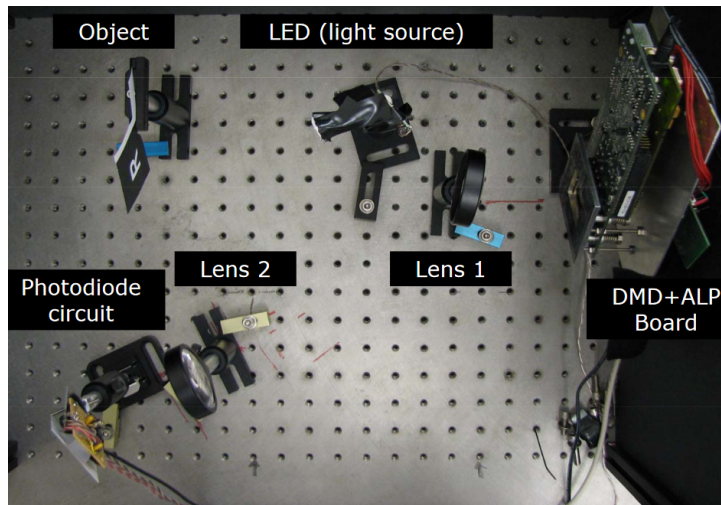
FIGURE 1.5: Laboratory prototype of a single-pixel digital camera. Target image is illuminated with light source and light-field is focused onto a DMD. Depending on every mirror orientation light is partially collected by a photodiode that integrates it into one measurement.

Researchers came up with a working prototype of a single-pixel camera (Figure 1.5). Essentially, it is an optical computer combining a single photon detector, A/D converter, two lenses and a DMD – digital micromirror device. DMD is an array of N programmable mirrors (N is also the number of pixels in the image) that can reflect light either on (value 1) or away from (value 0) the lens. Each mirror orientation is independent and changes (pseudo-)randomly every measurement.

The target image is illuminated with a light source and the light field is focused onto a

DMD. Depending on every mirror orientation light is partially collected by a photodiode that integrates it into one measurement. That way each of the $M \ll N$ measurements is the inner product $y_m = \langle \mathbf{x}, \boldsymbol{\phi}_m \rangle$ between the incident light-field from the scene under view $\mathbf{x}$ and a two-dimensional binary test function $\boldsymbol{\phi}_m$. After the M measurements are stacked together, they can be expressed as

$$\mathbf{y}^{M \times 1} = \boldsymbol{\Phi}^{M \times N} \mathbf{x}^{N \times 1} + \mathbf{e}^{M \times 1}, \tag{1.6}$$

where the *sensing* or *measurement matrix* $\boldsymbol{\Phi}$ provides a *dimensionality reduction* and is constructed as $\boldsymbol{\Phi} = [\boldsymbol{\phi}_1, \boldsymbol{\phi}_2, \ldots, \boldsymbol{\phi}_m]$. $\boldsymbol{\Phi}$ is said to be non-adaptive if it is fixed and does not depend on previous measurements. By appropriately designing $\boldsymbol{\phi}_m$ and using the l_1 optimization, a k-sparse image vector $\mathbf{x}$ can be reconstructed. This was well demonstrated by collecting random reflections from an image (256×256 pixels) and then unraveling these into real pixel intensities.

The single-pixel type camera reduces the complexity of a photon detector array down to just one unit. However, the DMD array size is a limiting factor for the maximum intrinsic resolution. This acquisition strategy clearly has potential for other wavelengths and video imaging, but currently in the ultrasound frequency band there are no ready-to-use hardware solutions or prototypes of this kind.

1.2.2 Multiply Scattering Medium

Another appealing approach for optical imaging was proposed by A.Liutkus *et. al* [16]. Featuring the idea of gathering information about the object in controlled, but pseudo-random fashion, they pointed out that carefully engineered hardware is needed to achieve randomization. To avoid using DMDs or metamaterials [17] they replaced emulated randomization by a natural multiply scattering material. In their experiments they used a 300 μm layer of Zinc Oxide (ZnO) or simply – white paint.

After entering the medium, waves experience complex interference and phase variation. This results in seemingly random measurements acquired by M sensors on the other side of the imaging system. Comparison between this approach, classical sampling and the single pixel camera is schematically shown in Figure 1.6.
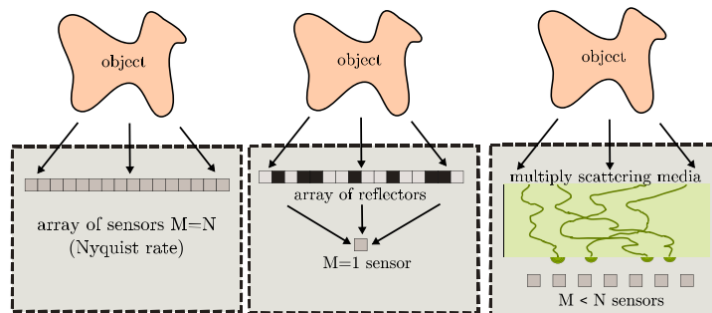
FIGURE 1.6: From left to right: classical sampling, emulated randomization (DMD), multiply scattering material

With respect to the diversity between an engineered CS mechanism and a truly random scheme, the latter one has several gains. Apart from being readily available, this sensing method has no constraint on the number of measurements taken in parallel. That is, M can be selected arbitrarily and it provides control over the experiment duration (note that we are bound to have a transmitter/receiver pair as one device to execute pulse-echo acquisition).

One complication that rises when using this approach, is that the randomization pattern is

no longer known *a priori* like the test functions ϕ_m in the single pixel camera case. To overcome this issue a calibration procedure is needed. The authors introduced "a measured Transmission Matrix" in order to deal with unknown randomization patterns. Basically, it is the same matrix from (1.6) linking all input-output wave fields, although, experimentally measured by using a spatial light modulator [18]. It has been shown that the transmission matrix is useful to focus through the scattering medium or detect objects on the other side of it.

1.2.3 Time Reversal Focusing

N.Etaix *et.al* [19] presented an idea of a low-profile acoustic imaging device with only one transmit/receive element. They exploit the *time reversal theory* to focus the transducer anywhere in a 3D volume. According to the theory, if the medium is reciprocal and the channel's impulse response is known, the latter can be re-emitted in time-reversed order. Mathematically, this results in the response auto-convolution [20]. Knowing that the auto-convolution has a peak in the origin, focusing is effectively achieved. The time reversal result is equivalent to matched filtering – energy maximization at the desired location in space and time.

Reciprocity is often a naturally complied property, but this method's weakness is the need to know all spatial impulse responses. This implies that the action sequence "transmit a pulse – record pressure at some point in space – move to the next point" should be repeated multiple times.

To avoid lengthy point-by-point measurements in 3D space, they proposed a synthetic algorithm and a modification to the circular transducer – a metal plate of chaotic geometry tightly coupled to the piezoelectric element and having a bigger area. The rigid metal plate acts as a hard wall and introduces the boundary condition to the mounted piston. The Rayleigh integral can be applied to compute the acoustic pressure at any point in front of the plate from the knowledge of its vibration pattern:

$$p\left(\boldsymbol{r}\right) = \frac{jw\rho}{2\pi} \int \int_S \frac{v_n\left(\boldsymbol{r}_s\right) e^{-jk|\boldsymbol{r}-\boldsymbol{r}_s|}}{|\boldsymbol{r} - \boldsymbol{r}_s|} dS, \tag{1.7}$$

where $\boldsymbol{r}_s$ and $\boldsymbol{r}$ denote the source and field points, w, ρ and k are respectively, the frequency (rad/s), the density of the medium and the wave number ($\frac{w}{c_0}$). p, v_n and S are the field pressure, the source normal velocity and the set of all points on the plane. This method exhibits quite high precision when compared with the straightforward microphone recording. In addition, the number of actual measurements was reduced to a 2D region of the plate surface. The authors experimentally proved the focusing method's potential in pulse-echo mode by imaging two scatterers in 3D space.

The work described in this paper not only has similar goals and conditions (circular transducer, acoustic domain), but also uses strongly related methods. The Rayleigh integral usage is equivalent to the angular spectrum approach, as it is described in Chapter 4. The chaotic cavity serves the same purpose as our mask. Its unusual shape increases the wavefront mode number and, consequently, the reconstruction quality.

Our approach differs in the fact that we do not try to focus at every point, but reconstruct the whole 3D volume at once by means of a mathematical model. Another distinction is practical – the aberration mask proposed by us is cheaper, smaller than the reverberant cavity and has better coupling with the medium.

Chapter 2

Single Element Imager

2.1   Matrix Model

This thesis aims to reconstruct a 3D volume using a single element transducer ($M = 1$). Let us consider a ROI discretized using a spatial grid with $N_s = N_x \cdot N_y \cdot N_z$ grid points. The received pulse-echo signal $y(t)$ is then given by the following formula:

$$y(t) = \sum_{i=1}^{N_x} \sum_{j=1}^{N_y} \sum_{k=1}^{N_z} \left[x_{ijk} \cdot a_{ijk}(t) \right] + n(t), \tag{2.1}$$

where a_{ijk} is the impulse response corresponding to the echo signal created by a unit strength scatterer on the grid position $[i; j; k]$, x_{ijk} is the scatterer's strength at that point and $n(t)$ accounts for the signal-independent noise in the system.

In case of a 2D (1D) region, one (two) of the dimensions' lengths N_x, N_y or N_z is (are) squeezed to only one point and the equation is simplified accordingly.

The model (2.1) gives a discretized linear spatio-temporal formulation of the imaging system. The signal $y(t)$ is a mixture of scaled and summed impulse responses, corresponding to non-zero pixels in $\mathbf{x}$.

By rearranging the terms in (2.1), and stacking them into vectors, we can write the discrete-time version of it

$$\mathbf{y} = \mathbf{A}\mathbf{x} + \mathbf{n}. \tag{2.2}$$

In this equation, $\mathbf{y} = [y(1), y(2), \ldots, y(N_t)]^T$ is the vector obtained by taking N_t samples of $y(t)$, $\mathbf{x} = [x_1, x_2, \ldots, x_{N_s}]^T$ is the vector of scatterer strengths at N_s grid positions, $\mathbf{n} = [n(1), n(2), \ldots, n(N_t)]^T$ is a noise vector, and the matrix

$$\mathbf{A} = \left[([\mathbf{a}_{111}, \mathbf{a}_{112}, \ldots, \mathbf{a}_{11N_z}], \ldots, [\mathbf{a}_{N_xN_y1}, \mathbf{a}_{N_xN_y2}, \ldots, \mathbf{a}_{N_xN_yN_z}]) \right]$$

is a system matrix, whose columns

$$\mathbf{a}_{ijk} = [a_{ijk}(1), a_{ijk}(2), \ldots, a_{ijk}(N_t)]^T$$

represent the N_t-point sampled impulse response obtained from $a_{ijk}(t)$. In other words, each column of $\mathbf{A}$ contains an echo from a unit scatterer at the corresponding pixel.

Equation (2.2) will be referred to as the imaging equation. The $N_t \times N_s$ system matrix $\mathbf{A}$ is the imaging operator or the $\mathbf{A}$-matrix. Image $\mathbf{x}$ is now a part of the formula, which can be solved using a variety of linear techniques.

FIGURE 2.1: System of linear equation written in matrix form: sensor observations $\mathbf{y}$, matrix $\mathbf{A}$ containing estimated echo signals from every pixel, unknown image vector $\mathbf{x}$, noise $\mathbf{n}$.

In this project, we counterbalance the absence of a multi-sensor probe with an aberration mask rotation. That is, 360 different $\mathbf{y}_m, \mathbf{A}_m$ pairs will be available for processing. This approach does not change the model as the vectors $\mathbf{y}_m$ and matrices $\mathbf{A}_m$ can be concatenated vertically to obtain the a similar expression as in (2.2):

$$\begin{bmatrix} \mathbf{y}_0 \\ \mathbf{y}_1 \\ \vdots \\ \mathbf{y}_{M-1} \end{bmatrix} = \begin{bmatrix} \mathbf{A}_0 \\ \mathbf{A}_1 \\ \vdots \\ \mathbf{A}_{M-1} \end{bmatrix} \mathbf{x} + \mathbf{n} \tag{2.3}$$

This model also applies if a transducer array ($M > 1$) is used or multiple pulses with several frequencies are transmitted. All methods achieve the same goal – to examine an object from different points of view. If $\mathbf{y}_0...\mathbf{y}_M$ provide independent information, the resulting $\mathbf{A}$-matrix will have lower coherence (the maximum absolute value of the cross-correlations between the columns of $\mathbf{A}$) than each of its sub-matrices.

2.2 Image Reconstruction Problem

The image reconstruction task, described by the model of the previous section, is an example of a *least squares* (LS) problem. The $\mathbf{x}$ vector is estimated by minimizing the following expression:

$$\underset{x}{\text{minimize}} \, \|\mathbf{A}\mathbf{x} - \mathbf{y}\|_2^2 \tag{2.4}$$

$\mathbf{A}$ is neither sparse, nor symmetric, nor squared. In this case, the naive LS solution

$$\mathbf{x} = \mathbf{A}^{-1}\mathbf{y} \tag{2.5}$$

cannot be used.

SVD

Of particular importance in solving rectangular systems is the *singular value decomposition* (SVD) [21, 22]. It provides a factorization for any non-square matrix $\mathbf{M}^{m \times n}$ given by:

$$\mathbf{M} = \mathbf{U}\mathbf{\Sigma}\mathbf{V}^{\mathbf{H}}, \tag{2.6}$$

where $\mathbf{U}^{m \times m}$ and $\mathbf{V}^{n \times n}$ are orthonormal matrices, $\mathbf{\Sigma}^{m \times n}$ is a diagonal matrix with elements called singular values.

The factorization can be used to compute a generalized inverse of $\mathbf{M}$ regardless of its rank and m/n ratio. The Moore-Penrose pseudoinverse [23, 24] $\mathbf{M}^{\dagger} = \mathbf{V}\mathbf{\Sigma}_e^{-1}\mathbf{U}^H$ ($\mathbf{\Sigma}_e$ is a square

subpart of $\boldsymbol{\Sigma}$) satisfies the condition $\mathbf{MM}^\dagger\mathbf{M} = \mathbf{M}$, and exists for any matrix. It equals $\mathbf{M}^{-1}$ in case $\mathbf{M}$ is invertible.

LSQR

The SVD method is robust, but in most cases $\mathbf{A}$ is of prohibitive size to perform the decomposition. Due to the high dimensionality of the problem, we are constrained to use iterative reconstruction methods. The most commonly used algorithms for large-scale linear problems are based on the *conjugate gradients* method – LSQR [25], LSMR [26].

The LSQR algorithm employs the Golub-Kahan bidiagonalization procedure [27]. At every iteration k, $\mathbf{W}_k^{m\times(k+1)}$, $\mathbf{P}_k^{n\times k}$, $\mathbf{p}_{k+1}^{n\times 1}$ and bidiagonal $\mathbf{B}_k^{(k+1)\times k}$ are computed such that:

$$\begin{cases} \mathbf{A}^T\mathbf{W}_k = \mathbf{P}_k\mathbf{B}_k^T + \gamma_{k+1}\mathbf{p}_{k+1}\mathbf{e}_{k+1}^T \\ \mathbf{A}\mathbf{P}_k = \mathbf{W}_k\mathbf{B}_k \end{cases}, \tag{2.7}$$

where $\mathbf{e}_k$ denotes the $(k+1)$-st standard unit vector and

$$\mathbf{B}_k = \begin{bmatrix} \gamma_1 & & & \\ \beta_2 & \gamma_2 & & \\ & \ddots & \ddots & \\ & & \beta_k & \gamma_k \\ & & & \beta_{k+1} \end{bmatrix}. \tag{2.8}$$

For reasonably small k, the matrix $\mathbf{B}_k$ approximates very well the matrix $\mathbf{A}$. Following that, a sequence of approximations $\hat{\mathbf{x}}_k$ are computed with the monotonically decreasing residual norm $\|\mathbf{y} - \mathbf{A}\hat{\mathbf{x}}_k\|_2$. As stopping criteria, the maximum number of iterations k_{max} or residual tolerance are used. The number of maximum iterations for the method plays an important role. Large values for k_{max} might lead to a corrupted $\mathbf{x}_k$, and too small values – to an over-smoothed solution.

One of the advantages of LSQR is that it only needs a few vectors of working storage (no big matrices are stored in memory) and uses $\mathbf{A}$ and $\mathbf{A}^T$ for matrix-vector multiplication, but do not modify the matrices themselves.

Regularization

The complexity of the problem arises not only from its dimensionality, but also from the (ill-)conditioning of the $\mathbf{A}$-matrix. This property of the matrix denotes a system's stability, i.e., how much the solution $\mathbf{x}$ changes with respect to a small change in $\mathbf{y}$. Numerically, it is expressed as the ratio between the maximum and minimum singular values – the condition number:

$$\kappa(\mathbf{A}) = \frac{\sigma_{max}}{\sigma_{min}}. \tag{2.9}$$

If σ_{min} is magnified several orders (during inversion), the produced estimate $\hat{\mathbf{x}}$ will be far from the real $\mathbf{x}$. While a well conditioned $\mathbf{A}$ has $\kappa(\mathbf{A})$ close to 1, the typical values of our matrices can reach 10^9. For such high $\kappa(\mathbf{A})$ values, the solution is considered to be unstable.

In order to stabilize it, several regularization methods can be applied. *Tikhonov regularization* [28, 29] is a widely used method belonging to the l_2-norm based algorithms. This type of regularization imposes an additional quadratic constraint on (2.4). This leads to the following optimization problem

$$\underset{x}{\text{minimize}} \, \|\mathbf{A}\mathbf{x} - \mathbf{y}\|_2^2 + \lambda\|\mathbf{x}\|_2^2, \tag{2.10}$$

where the first term denotes how the solution fits the data and the second term penalizes solutions of higher norms to suppress noise components. The parameter λ is used to regularize the solution, and it weights the importance of the two terms. This is equivalent to assigning

the following weights to every singular value:

$$\hat{w}_i = \frac{\sigma_i^2}{(\sigma_i^2 + \lambda^2)}. \tag{2.11}$$

A special case of Tikhonov regularization, where the weights are either 0's or 1's, is called *truncated SVD* (TSVD):

$$\widehat{w}_i = \begin{cases} 1 & \text{if } \sigma_i > \tau \\ 0 & \text{if } \sigma_i \leq \tau \end{cases}, \tag{2.12}$$

with τ being a hard threshold regularization parameter.

In order to avoid computing the SVD, the problem from (2.10) can be reformulated, using the fact that for any two vectors $\mathbf{a}_1$ and $\mathbf{a}_2$:

$$\left\| \begin{pmatrix} \mathbf{a}_1 \\ \mathbf{a}_2 \end{pmatrix} \right\|_2^2 = \begin{pmatrix} \mathbf{a}_1 \\ \mathbf{a}_2 \end{pmatrix}^T \begin{pmatrix} \mathbf{a}_1 \\ \mathbf{a}_2 \end{pmatrix} = \mathbf{a}_1^T \mathbf{a}_1 + \mathbf{a}_2^T \mathbf{a}_2 = \| \mathbf{a}_1 \|_2^2 + \| \mathbf{a}_2 \|_2^2. \tag{2.13}$$

Then (2.10) becomes simply

$$\min \left\| \begin{pmatrix} \mathbf{A} \\ \lambda\mathbf{I} \end{pmatrix} \mathbf{x} - \begin{pmatrix} \mathbf{y} \\ \mathbf{0} \end{pmatrix} \right\|_2 \tag{2.14}$$

and can be supplied to any algorithm for solving iterative LS problems in order to find a solution $\hat{\mathbf{x}}$ without the need to compute the SVD. However, it is still required to find a suitable value for λ (or τ), which is not a trivial task. No reliable and automated parameter-choice algorithm exists, but the *L-curve criterion* and *generalized cross-validation method* heuristically proved their efficiency for several problem types.

Summarizing, the matrix ill-conditioning is related to the number of linearly independent columns in $\mathbf{A}$ and is a limiting factor for finding a stable (unique) solution. That is, if the columns are strongly correlated, any reconstruction method will have problems when deciding which of them to select (more than one possible solution). To alleviate this problem, in this work a strategy to increase the orthogonality of the columns in $\mathbf{A}$ is introduced.

2.3 Spatial Field of the Transducer

After a single element transducer emits a wave at a given pulse repetition frequency (PRF), it is switched to receiver mode and records the echo. By knowing the delay between the wave emission and echo reception (and also the speed of sound c_0), we can calculate distances to reflective obstacles (Figure 1.3a). The direction from which the echo arrives cannot be defined, as only one reference point is considered and no beamforming can be performed.

Figure 2.2 illustrates the problem. The transducer was immersed in water and an echo from a scatterer was recorded (the data acquisition process is outlined in Section 2.6). If the scatterer is moved from point to point in one plane and echoes are captured systematically, an intensity map or, *beam profile* of the transducer can be obtained.

An example of such a beam profile is shown at the top part of Figure 2.2. Every point's brightness represents energy (in dB scale) of the received signal. It is clearly seen that the transducer has a rounded symmetrical beam profile in the plane perpendicular to its axis. This is exactly what manufacturers desire to achieve – ideal directivity, intensity and uniformity of piezo-electrical elements.

The bottom frame of Figure 2.2 provides example echoes for a scatterer at the grid points
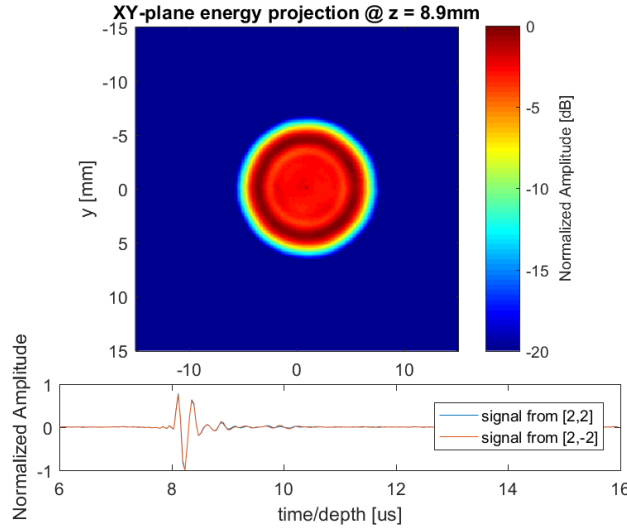
FIGURE 2.2: Top: energy-based beamprofile taken at 1 cm from the transducer surface (no aberration mask). Bottom: echo signals from two points equally distanced from the center.

[2;2] and [2;-2]. These locations are equidistant from the center and the signals are identical. In fact, all points forming a circle of an arbitrary radius around the [0;0] pixel are non-distinguishable by their echoes. Ambiguity is one of the main problems we address in this thesis. We want to retrieve a system matrix in which every column is unique. That would solve the problem of ill-conditioning too.

Neighboring columns' correlation also highly depends on the grid spacing (denoted by dx, dy and dz accordingly). A coarse grid implies less columns in $\mathbf{A}$, leading to less coherent dictionary and faster imaging, but the image resolution is not good. Computational speed, indeed, becomes an issue with $\mathbf{x} \in \mathbb{R}^{10^5}$.

On the other hand, having a high spatial sampling leads to the pixel duplication effect. Consider the case of a fine grid and a real scatterer laying between pixels. After the reconstruction, multiple non-zero pixels can be observed around the scatterer position, but with decreased amplitudes with respect to the real one. In our experiments, the region was divided into sub-wavelength-sized pixels in order to minimize this kind of complications. In addition, as shown later, a hydrophone membrane used during the calibration procedure has size comparable to the grid.

2.4 Aberration Mask with Rotational Freedom

The spatial field produced by the transducer provides information that is beneficial for reconstruction. However, the figures above show that the "ideal" spatial field is too ambiguous for this task. Classical information theory in this case encourages us to increase the entropy of the system.

> Idea: modify the transducer's spatial field deliberately, so that every point has a unique scattering pattern.

We can achieve this by introducing an *aberration* layer between the transducer and the medium.

In standard medical ultrasound, focusing on transmission and reception is performed assuming that the propagation medium is homogeneous and isotropic, where the Born approximation is valid. Aberration might be viewed as a deviation from this hypothesis.

Although research on estimation and correction of the aberration is constantly pursued, the core idea of this thesis, on the contrary, is to design a mask that promotes distortion to passing ultrasound waves. The simplest implementation of this idea would involve a plastic layer of uniform height with one (or several) holes in it (Figure 2.3). The mask (blue) is mounted in front of the transducer surface (yellow) and when this imaging device is immersed in water, the liquid fills the holes. Due to the ultrasound propagation speed difference in the two mediums, a complex interference pattern changes the propagation process of an echo coming from an object and returning back to the transducer (again through the mask). To use this information for the object reconstruction, we need to know the interference mechanism. In Section 2.6 we show that a calibration step – mapping a temporal response to every pixel – provides a practical solution.
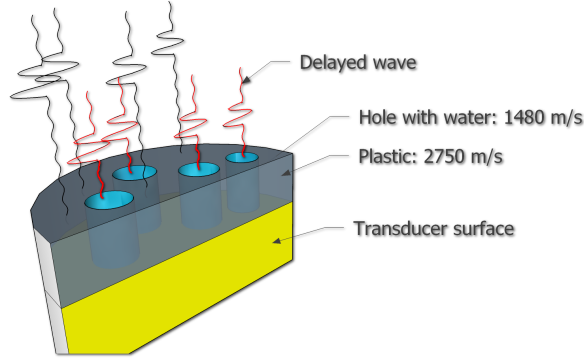

FIGURE 2.3: Main idea behind the aberration mask: spherical wave from the transducer is split in many sub-waves delayed according to the medium they are squeezing through.

Figure 2.4 provides a visual proof of the aforementioned idea. As Figure 2.2, it is a projection of all signals over time to a plane in space, but measured with the mask on the transducer. This time we see that the beam profile has lost its symmetrical shape and two echoes from the test positions are more different.
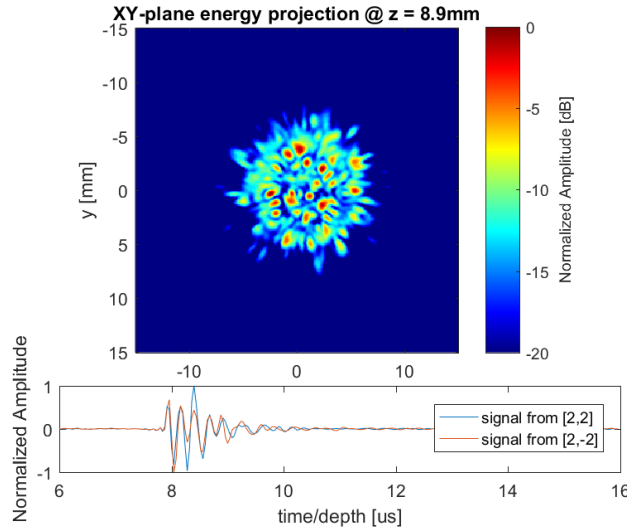
FIGURE 2.4: Top: energy-based beam profile taken at 1 cm from the transducer surface and applying the mask. Bottom: echo signals from two points equally distanced from the center

In case of a static mask, each measurement y_m is one time-sample of an echo signal and the number of measurements we can make is strongly limited by the echo length and the sampling frequency F_s of our choice. With a 5 MHz transducer and $F_s = 25$ MHz, the echo is ≈ 150 samples long. That makes the system of equations under-determined (having more column-pixels than row-measurements). Compared with the single pixel camera again, a DMD array has $N!$ states, possibly providing new information with N being the number of mirrors.

> Idea: by rotating the mask we also rotate the spatial field of the imaging device, thus providing a different view of the object.

Indeed, if several pixels have non-orthogonal responses even with the aberration mask, their correlation can be decreased if the mask is rotated by ω degrees. In theory we can divide 360° into as many parts as needed in order to achieve any number of measurements. In practice, we are limited by the rotation motor precision. In addition, we also have to consider the trade-off between the amount of new information (in relation to what we already have) and the computational resources we possess.

In case of an ideal transducer (absolutely uniform directivity and intensity over the aperture), its beam profile will not qualitatively change by rotating the mask by ω degrees. Predicting its new state is as easy as to rotate the initial 0 degree beam profile image by ω degrees. That means we only need the initial $\mathbf{A}_0$ and all $\mathbf{y}$'s to construct the model as in Equation (2.3).

In real life no transducer has ideal characteristics. The consequences of this are discussed in Section 2.6.1.

2.5   Building the A-matrix

The task of building the imaging operator has primary importance in this work. We investigated two approaches: fully experimental and prediction-based.

The former means: using a single point scatterer placed in the ROI, for different positions, each echo signal is measured one at a time, and corresponding $\mathbf{A}$ column is filled. The whole procedure is repeated as many times as we need pixels. The setup and data acquisition process are outlined in Section 2.6. Chapter 3 describes several designing issues faced when using this approach and presents the results. This way of performing imaging proved to be feasible, however the process can require a considerable amount of time as it requires previous knowledge of the impulse responses in a 3D volume.

In order to overcome the inefficiency of measuring a 3D $\mathbf{A}$ matrix of realistic size pixel by pixel, we devised a prediction-based method. Instead of recording pulse-echo traces, we propose to measure the ultrasound field pressure with a hydrophone. When we have a forward propagation pattern in some plane, we make use of the *angular spectrum approach* (ASA) to model the pressure distribution at any point further in depth. The theory behind the ASA is explained in Chapter 4. We cannot state that this method is a pure simulation model, as it still requires a source plane to be measured. Moreover, our imaging device is pulse-echo based. Hence, it is not only needed to predict forward pressure, but also to propagate it back to the transducer. Assuming that the *reciprocity condition* [20] holds, pulse-echoes are estimated using the auto-convolution function and the forward field.

Considering the $\mathbf{A}$ matrix acquired using the experimental approach, there is another interesting attribute of the model – usually the $\mathbf{A}$ matrix in the $\mathbf{Ax} = \mathbf{y}$ system is assumed error-free and noise-free. However, this does not always hold. As both $\mathbf{A}$ and $\mathbf{y}$ are measured variables, they are equally prone to measurement noise. That is, if we multiply a perfect image $\mathbf{x}$ by $\mathbf{A}$, we will not obtain the measurements $\mathbf{y}$. Errors-in-variable regressions, for instance, total least squares [30] (TLS), account for noise in independent variables when searching for an optimum solution. Although it could be beneficial to use those methods for reconstruction, unfortunately, they require the full SVD decomposition of $\mathbf{A}$.

2.6 Experimental Setup
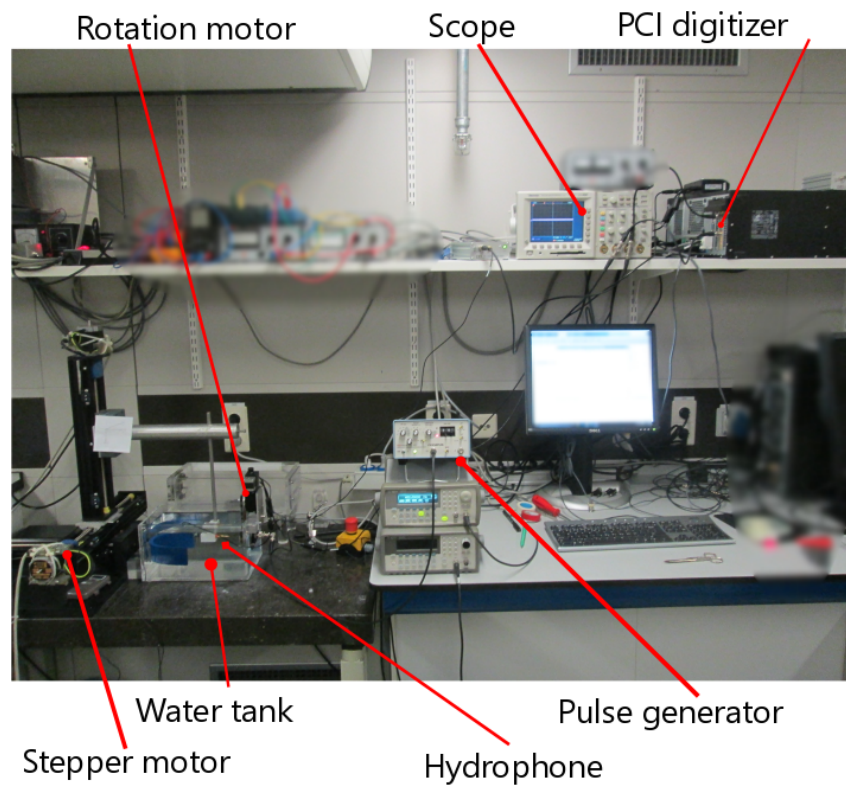
2.6.1 Pulse-echo Measurements
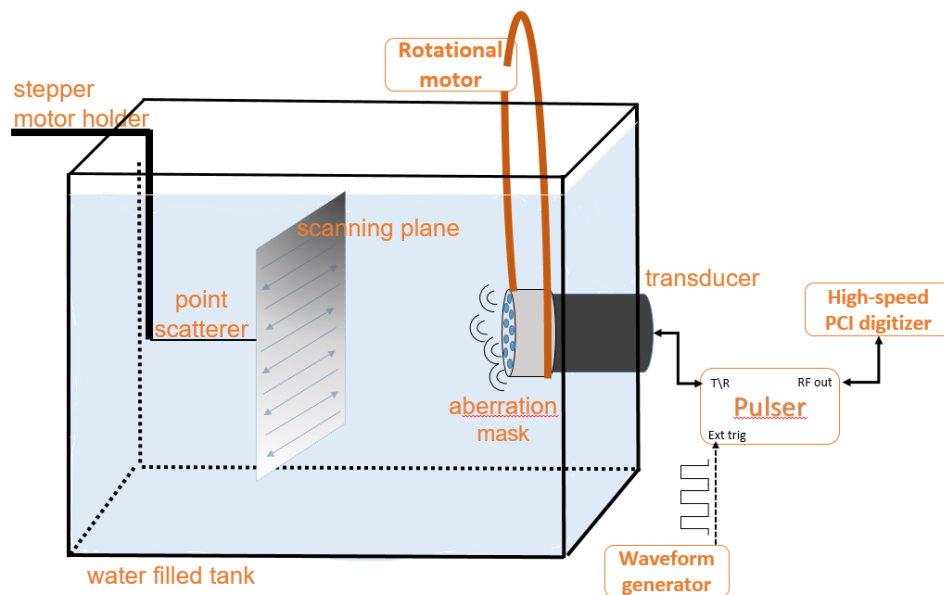

FIGURE 2.5: Experimental setup photo.

FIGURE 2.6: Schematic overview of the setup

As stated in the previous section, we aim to consecutively measure an echo from a single scatterer located in every grid point. From this data, we define our dictionary – the **A**-matrix.

Single Point Scatterer

A single point scatterer – an infinitely small inhomogeneity is, of course, unrealistic. In practice, we used a thin needle with a steel ball on the top (Figure 2.7). The scatterer size plays an important role – ideally, it should occupy one cell. The ball we use has a diameter of approximately 1 mm or 3λ (if a 5 MHz transducer is used). All measurements were performed in water. To avoid a highly undesirable effect of bubble scattering, water must be clean and bubble-free. A photo of the system is shown in Figure 2.5, and the main equipment devices are depicted in a simplified manner in Figure 2.6.

FIGURE 2.7: Single point scatterer used in experiments

All devices are connected by means of coaxial cables with BNC plugs. Some of the settings varied slightly from test to test, but the specifications listed here are considered the norm. In case of significant changes, they will be mentioned within the relevant section.

Pulser

In this project, pulsed ultrasound waves are sent into the medium. By means of a square-wave pulser/receiver (PANAMETRICS 5077PR), the transducer was excited with 300 V. Afterwards, an electrical signal generated from a backwards-propagated echo was read (Figure 2.8). The pulser was linked to the transducer through the input/output connection. In addition, it has an external trigger input and two outputs – trigger synchronization and RF$_{\text{out}}$.

FIGURE 2.8: Pulser/Receiver

Waveform Generator

A programmable waveform generator Agilent 33220A (Figure 2.9) is used to trigger the pulser. It was configured to produce squared 1 μs wide pulses with $PRF = 400$ Hz.

FIGURE 2.9: Waveform generator functioning as a trigger

Transducer

Experiments were performed with a single element immersion transducer (Figure 2.10). This type of sensor is particularly designed to be partially or fully immersed in water and is acoustically matched to it. We tested unfocused transducers with 0.5" aperture diameter and several operating frequencies (2.25 or 5 MHz). Results presented in this report are produced by the 5 MHz transducer, as it provides higher resolution in exchange for shallower penetration depth and higher sampling rate.

FIGURE 2.10: Single element immersion transducer

PCI Digitizer

After sending an ultrasound pulse, the transducer switches to the receiving mode and passes the incoming pressure back to the pulser in the form of a continuous voltage signal. The signal is transferred directly to the digitizer where it is sampled and stored in computer memory. For us, the most important characteristic of the digitizer is its resolution – the smallest signal change that it is able to detect.

FIGURE 2.11: Acqiris DP310 digitizer

Measured signals are expected to be quite weak and disrupted by noise. It is essential to adjust the dynamic range correctly. If one overestimates the range, one can easily loose a couple of bits. On the other hand, by setting a very small range, the signal can be clipped and the measurement becomes invalid.

We used a 12-bit Acqiris DP310 digitizer mounted in a PC. It has 4096 discretization levels providing resolution of voltage differences larger than 1.2 mV (in case of 5 V vertical range).
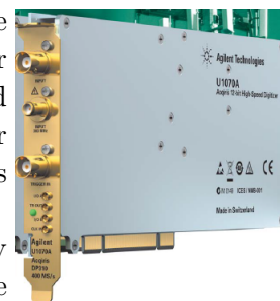
Stepper Motor and High-Speed Acquisition

To perform automated and precise movement a 3D stepper motor is used.

In fact, the number of measurements to be taken is dependent on the transducer's frequency – at least two data points per wavelength. The 5 MHz transducer emitted waves are 300 μm long and for a quite moderate imaging region of 3×3 cm the number of imaged pixels ascends to at least 40.000.

For the sake of time efficient acquisition, measurements are performed simultaneously with the motor's continuous movement. The point scatterer moves at a constant speed of 20 mm/s until it reaches the end of the assigned region. Then, the scatterer is pushed to the next line and moves in the opposite direction (as the arrows show in Figure 2.6). At the same time, the transducer shoots acoustic pulses and the echoes are recorded.

The PRF has to be selected appropriately: for example, if it requires 1.5 seconds $\left(\frac{3 \text{ cm}}{20 \text{ mm/s}}\right)$ to move along one line and 300 (3 per λ) measurements are necessary, then the PRF $= 300 \cdot 1, 5 = 200$ Hz. To fully characterize the transducer's spatial field in one 2D plane (9 cm^2) it takes approximately 15 minutes. Note that this has to be done only once. The recorded interference pattern is unique for the particular transducer and the mask.

It is crucial for successful imaging to have a precise $\mathbf{A}$. No matter which method we choose for building it, additive noise in the dictionary is very undesirable. The drawback of fast-scanning is that no signal averaging can be done for reduction of measurement noise. A point-to-point scan, when the motor is static while measurements are taken, would allow to perform averaging on every signal.

Rotation Motor

In order to take measurements $\mathbf{y}$ for different angular positions of the mask, the mask is rotated by means of a motorized rotary stage Zaber T-RS60A (Figure 2.12) and a rubber band. According to (2.3), if we rotate the mask one full circle and capture data every degree, then $M = 360$. It is important to investigate the rotational variance provided by the mask, i.e., how fast does the echo changes or how different are two echoes from, lets say, $90°$ and $91°$. In this thesis the terms *mask angle* and *mask position* are used interchangeably.

In theory, to generate $\mathbf{A}_1 \ldots \mathbf{A}_{M-1}$ and make the system of equations consistent, we only require $\mathbf{A}_0$. Any degree replica of it can be produced by rearranging columns. Two beam profiles taken at 0 and 90 degrees should completely overlap if appropriately rotated. In practice, due to non-uniformities in the transducers, we have reasons for actually measuring several $\mathbf{A}$-matrices (for example, $\mathbf{A}_0$, $\mathbf{A}_{90}$, $\mathbf{A}_{180}$ and $\mathbf{A}_{270}$).

First of all, it is impossible to manufacture an ultrasound transducer with absolutely uniform sensitivity. Secondly, the mask can not be fixed on the transducer, it must stay flexible. As a result, there might be

FIGURE 2.12: Rotary stage in work: 360 echoes from a single point scatterer are recorded.

a micrometer range gap between the transducer surface and the mask. Figure 2.13 shows the consequences of those technical issues. The beam profile taken at $0°$ ($\mathbf{A}_0$) and rotated by $90°$ by means of the MATLAB function *imrotate()* ($\mathbf{A}_{90r}$) is not equal to the one taken at $90°$ ($\mathbf{A}_{90}$). The residual $\mathbf{A}_{90r} - \mathbf{A}_{90}$ is shown at the most right plot.

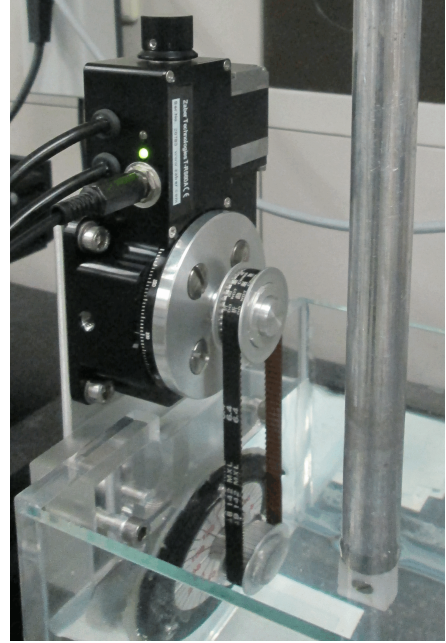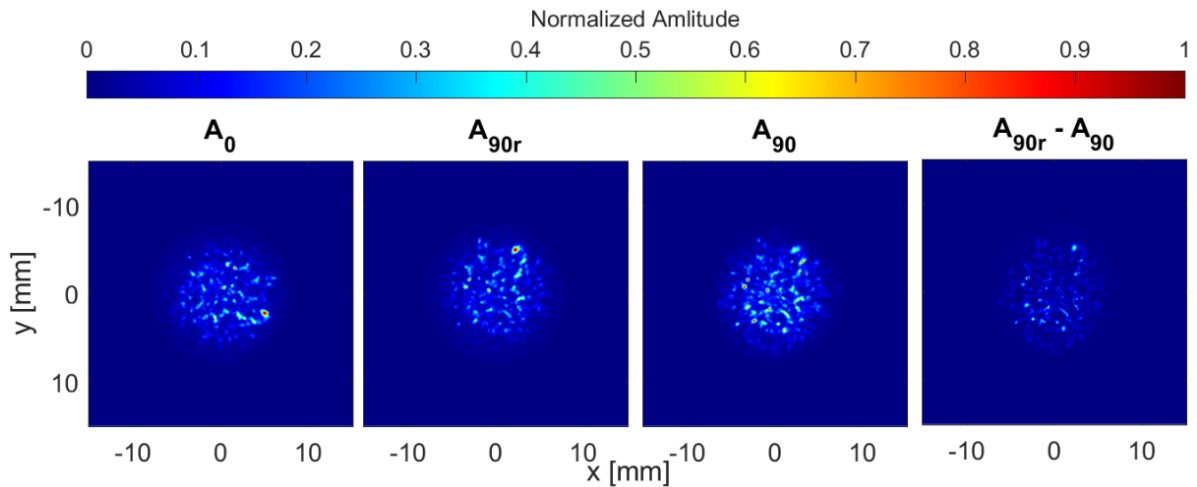FIGURE 2.13: Beam profiles illustrate the "transducer-mask" system asymmetry. From left to right: $\mathbf{A}$ measured at $0°$, imrotate($\mathbf{A}_0$,90), $\mathbf{A}$ measured at $90°$, absolute difference between $\mathbf{A}_{90r}$ and $\mathbf{A}_{90}$.

2.6.2 Hydrophone Measurements

In later stages, we modified our approach to defining the **A**-matrix (Chapter 4) and opted for recording ultrasonic pressure at pixel locations instead of signals received by the transducer. The acquisition process remained the same, except that instead of the point scatterer model, a broadband (0.5-20 MHz) hydrophone needle (Figure 2.14) with 0.2 mm membrane was used.
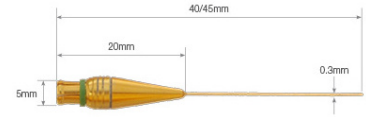

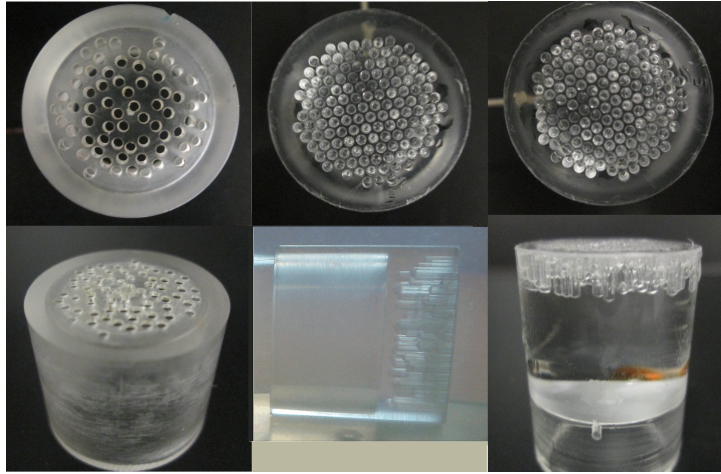
FIGURE 2.14: Hydrophone.

2.7 Mask Design Choice

FIGURE 2.15: Examples of masks designed. Left: randomly located holes in PMMA material. Center: randomly located random length deepenings in PMMA. Right: similar to the previous one, but an additional layer of solid PMMA is added.

The choice of the mask design has a significant role. In the absence of the mask, bare transducer's "field of view" is defined by its central frequency, aperture size and directivity pattern. The mask, due to its acoustical properties, might affect, for example, effective imaging depth. From the reconstruction side, there is a strong desire to make a system matrix **A** computationally stable for inversion. This means that it should have a condition number close to one (flat SVD spectrum).

We proposed several models (Figure 2.15), gradually increasing design complexity. All masks are made from Acrylic glass (Polymethyl methacrylate or PMMA) with the speed of sound $c_{PMMA} = 2750$ m/sec. The first design – randomly located holes (diameter 1 mm) in PMMA. The possible parameters for this case are thickness of the material, holes distribution and diameter. The mask provides two levels of phase shifts - the wave goes either through plastic or water.

The second variant – instead of holes, random length deepenings were made (variable value for the phase shifts). By introducing a multi-level aberration layer we expect to increase the orthogonality of **A**'s columns.

The third design – the aberration interface coupled with a much thicker bulk piece PMMA – was encouraged by the transducer asymmetry in rotation. Imperfections as in Figure 2.13 are less pronounced in depth than in the near-field. Waves travel fast through the solid part unaffectedly until they reach the aberration interface. By changing the solid part length, minimal imaging depth is controlled.

In order to evaluate different masks, for each of them we have recorded the pressure field in a plane perpendicular to the acoustic propagation axis. Figure 2.16 shows one slice through the recorded 3D spatio-temporal matrix. As the plane was taken at the same distance in all cases, we can notice how the mask design affects the received echo signals. The higher speed of sound in the PMMA forces echoes to come back faster than without the mask. At the same time, signals are also attenuated more (compare the color bars' limits), hence energy throughput and the SNR are reduced. In addition, more phase shift levels make the echo signals longer, which can be relevant for resolution enhancement.
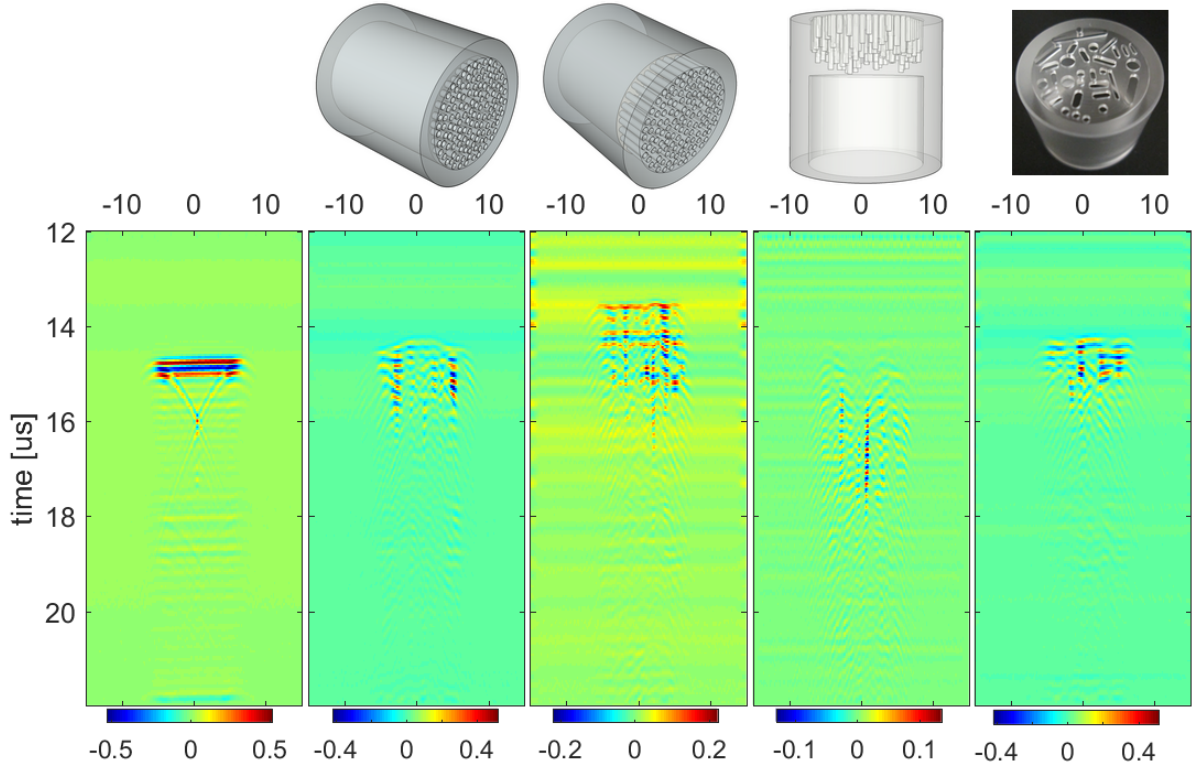
FIGURE 2.16: Received RF for various mask designs. From the left: bare transducer, 0.5 mm mask with holes, 2 mm mask with holes, random phase shift mask, 1 mm mask with various shaped slits.

A matrices were built from these RF signals and their $\kappa(\mathbf{A})$ was chosen as a quantitative measure for the mask optimality. $\kappa(\mathbf{A})$ evaluates the imager in general, independently of the equation's left-hand side **y**. The results (Figure 2.17) show that the mask with maximum phase shift levels provides 10 time less correlated impulse responses.

Judging from the last mask with the various-shaped slits, it seems that the on-surface pattern does not play a big role. This is not entirely true. One should not forget the rotation effect, during which the figures move with different angular speeds and provide extra information.

FIGURE 2.17: Mask design vs condition number. The highest condition number is 7.45×10^3.

A static aberration mask is cheaper and simpler than any electronic device, but spatial

diversity can be accomplished in other ways too. It can include electronic or mechanical elements. For instance, using two electro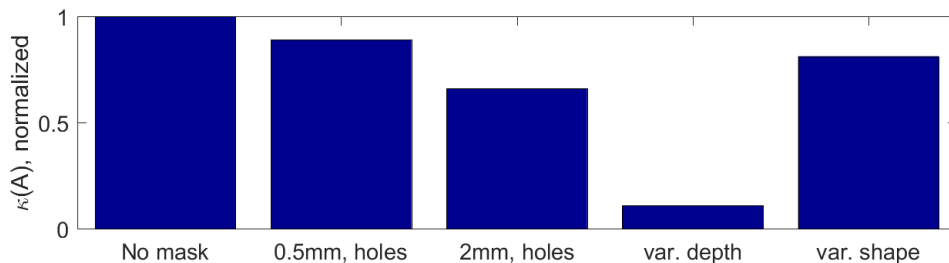des the mask can be heated from inside. If it is filled with liquid or other temperature-dependent material, this will provide a desired randomization effect. Furthermore, instead of a single pulse, a sequence of pulses with different f_0 can be transmitted into the medium. This provides another degree of freedom and can substitute the need of rotation or complement it.

The only absolute requirement for the mask is the scattering pattern reproducibility. The way it changes the spatial field should be under control, otherwise $\mathbf{A}$ will be different every measurement. The ability to simulate the mask effect with high precision would be a desired feature for research and analysis.

In the following chapters, results were produced by the mask with variable depth deepenings. It looks like an obvious choice from the previous figure. Although this mask can be thought of as the obvious choice, due to its conditioning, there are several disadvantages also. Firstly, this mask attenuates ultrasound more than other masks, which is undesirable when the way we perform the calibration is taken into account: electronic noise and the motor oscillations alter weak signals. The second disadvantage of the mask is related to the *ringing effect* explained in Section 3.1.

Chapter 3

Constructing the A Matrix by Measurements

This chapter presents a reconstruction example achieved by performing a complete experimental calibration procedure – all columns of the **A** matrix were directly measured. As building the 3D **A** matrix by measurements requires a considerable amount of time, we decided to begin with a simpler case involving a single plane. In this case, the object must also be positioned in the same plane while acquiring **y**. Success in the reconstruction demonstrates the concept's potential, and provides initial results that can be further analyzed for future improvements.

3.1   Post-processing

After source to point impulse responses at one plane have been measured, the data needs to be processed before the actual reconstruction can be done. The measurements lead to a 3D (two spatial dimensions + time) array filled with RF signals (a slice of the array for fixed x-axis is shown at Figure 3.1b). After reshaping the data, it becomes a two-dimensional **A**-matrix relating a temporal signal to every spatial point.

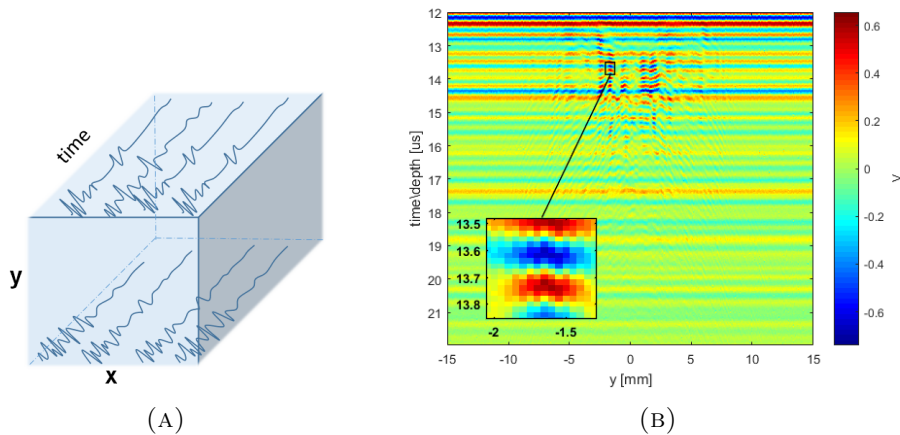(A)   (B)

FIGURE 3.1: (A) Measurement result (simplified visualization): every pixel scanned has a corresponding voltage signal.
(B) Data slice over one of the spatial dimensions and (secondary axis) motor movement artifact.

Motor Fluctuations

Fast data acquisition comes at the price of signal oscillations introduced by the stepper motor's movement. Secondary (zoomed) axis at Figure 3.1b shows this undesirable effect. Its influence can be reduced by applying a low-pass filter in the Fourier domain.

Ringing

Another practical concern worth to mention is an extension of the so-called "ringing effect" [31]. After generation of ultrasound, waves are emitted into the medium, but also internally into the substrate of the transducer. Internal resonance increases the duration of the emitted pulse. As a result, transducers cannot reliably sense a reflection from a target closer than a critical distance, i.e., where the received wave's magnitude exceeds that of the emitted wave. Nowadays these residual oscillations are suppressed effectively by acoustic/mechanical (backing materials) or electrical (passive circuits) means.

Adding an aberration layer gives rise to a new ringing process. As can be seen from Figure 3.2 (also at Figure 3.1b – horizontal lines of higher amplitudes than the echo), the mask itself introduces a high amplitude signal that is received long after the actual excitation pulse was sent. Notice also the trend, that if a more complicated mask design is used, the ringing spreads further.
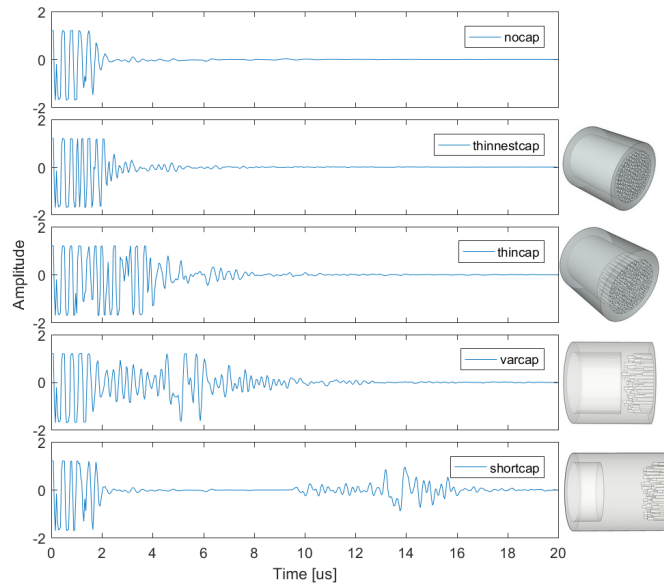
FIGURE 3.2: Received echo-signal when there is no scatterer present, for several mask designs. From the top: 1st – no aberration mask; 2nd – simple mask with 0.5 mm thickness; 3rd – simple mask with 3 mm thickness; 4th – second type mask (with variable deepenings); 5th – third type mask (1 cm thick solid PMMA);

High ringing can be named as "the mean signal" as it is received by the transducer independently of the imaging object (even if there is no scattering at all). This issue has several degrading effects for the project. At depths smaller than 1 cm, weak received signals are masked by the ringing, so that our digitizer's resolution is spent non-effectively: all bits are used to sample a large signal, however, only the smallest part of it contains useful information.

The greatest problem is that the presence of ringing ruins the superposition assumption in our model. Every column of the **A**-matrix is a sum of a constant ringing signal and some received echoes as shown in Figure 3.3a (these are not real signals, but abstract visualization of the problem). Then, according to the superposition principle, if only one pixel is active in

the image $\mathbf{x}$, and it has brightness 2, a receiver would record the $\mathbf{A}$-matrix column scaled by two – blue line at Figure 3.3b. But in reality, because of the constant nature of the ringing, the receiver will display the red signal at the same picture. Reconstruction, of course, will happen with major errors. This explains why it cannot be left in $\mathbf{A}$-matrix (linearity is ruined).
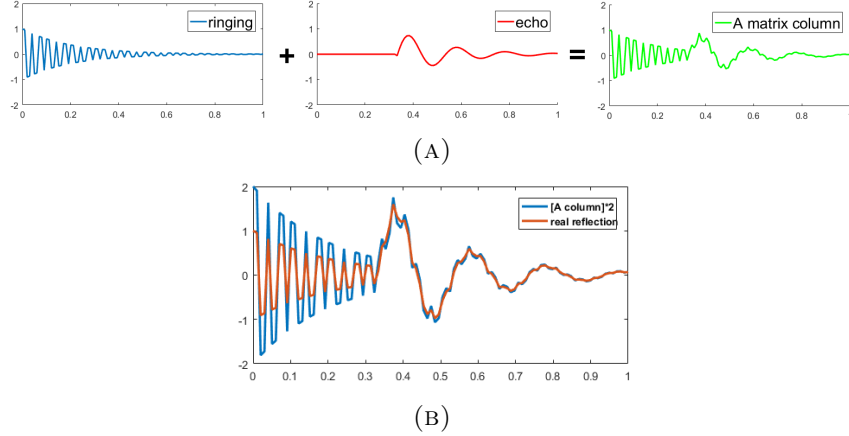

(A)

(B)

FIGURE 3.3: (A) Ringing provoked by the emitted pulse back-and-forth propagation "in the mask" (left) and an echo produced by a scatterer (center) constitute one $\mathbf{A}$-matrix column (right). (B) Visualization of the ringing signal non-scalability to the number of single scatterers.

In the sense of minimizing the ringing, the mask of our choice is not optimal. As it is seen from Figure 3.2, the mask we use shows just the highest relative ringing.

A possible solution is to subtract the mean signal in order to make an $\mathbf{A}$-matrix properly scalable. In order to do so, we prerecord $\mathbf{y}_r$ in absence of any scatterer for all 360 degrees. Basically, we perform measurements on an empty volume. Before the reconstruction $\mathbf{y}_r$ is subtracted from both the dictionary $\mathbf{A}$ and measurement $\mathbf{y}$ to work with clean echoes.

3.2   Letter Reconstruction

After initial processing is done, we proceed with the reconstruction. It is common to image a letter in such proof-of-concept projects [32]. We 3D-printed several letters (Figure 3.4a) and sprayed metal powder on them (Figure 3.4b) to increase acoustical reflection capability. Capital letters have a size of approximately 4×2 mm.
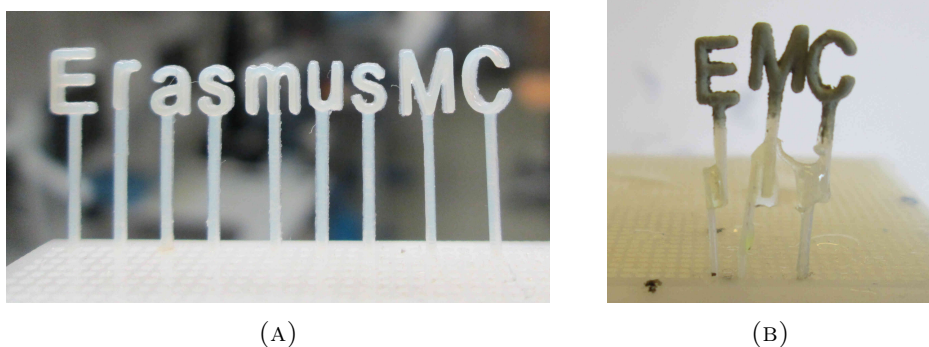

(A)

(B)

FIGURE 3.4: (A) A set of 3D-printed letters.
(B) 3D-printed letters covered with metal powder for better acoustical reflection.

The letter "E" was placed in the scanned plane while rotating the mask. A set of $M = 360$ $\mathbf{y}_m$ measurements were recorded (Figure 3.5) with a sampling rate of 25 MHz. We restricted the

imaging region to an area of 10×10 mm (10.000 pixels). Using a wider ROI does not provide further insights, because a single element emitted energy does not reach farther. This behavior is proved by the beam profiles shown previously (Figure 2.4).
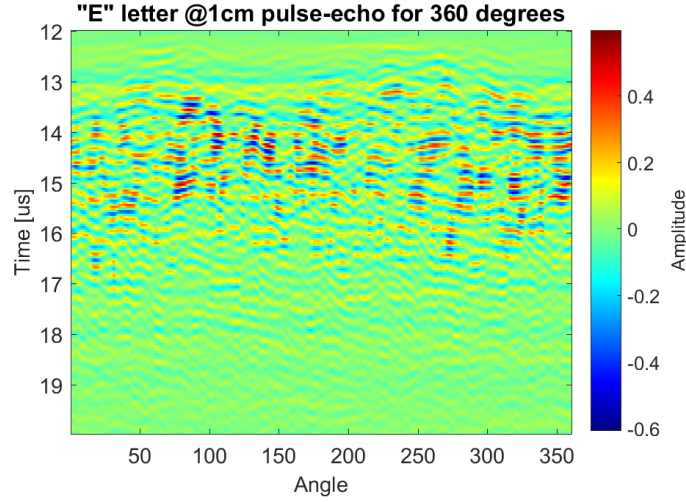
FIGURE 3.5: 360 reflections of the letter taken for every mask rotation angle.

The **A** matrix, which corresponds to the above mentioned numbers has size $360 \cdot N_{samples} \times 10000$. To be more efficient in time and reduce computational resources, we must search for opportunities to reduce the problem size. Observing Figure 3.5 it came to our attention, that the dimensionality can be reduced in two ways.

We can truncate the echoes only to the part where strong variability and amplitude is noticed (in this particular case – from 13 us to 16 us), reducing the total number of equations.

Another way is to not use all 360 signals, but a fraction of them. This seems reasonable, as it is seen that **y** changes rather smoothly. The cross-correlation matrix of **y** (Figure 3.6) confirms the idea that every three (or more) adjacent angles are highly correlated. This provides a valid approach to observe, how much diversity the mask provides. For reconstruction, every n^{th} ($n = 1, 2, 3, 6, 8, 12$) angle is taken until proper image quality is achieved. Note that in the ideal case the cross-correlation matrix is the identity matrix.

FIGURE 3.6: **y** cross-correlation matrix: every pixel denotes the similarity between two echoes measured for different mask positions.

In Figure 3.7 the reconstructed letter, depending on the number of rotations used, is shown. The best reconstruction in terms of quality and noise is achieved at approximately 100 angles,

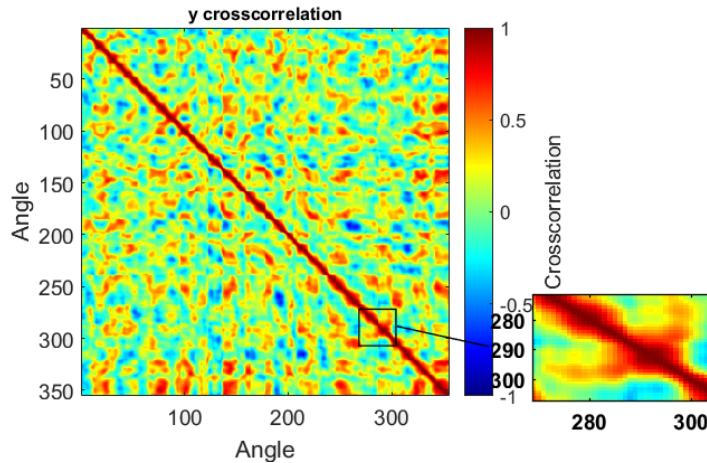which confirms the idea that only every 3rd or 4th measurement provides new information.

Experiments also show that our problem is so ill-posed, that the maximum number of iterations has to be between 5 and 10. This appears to be the main stopping criterion for the algorithm. Further optimization leads to overfitting (error modeling), because for noisy data the LS residual $||\mathbf{A}\hat{\mathbf{x}} - \mathbf{y}||_2$ never goes to zero.
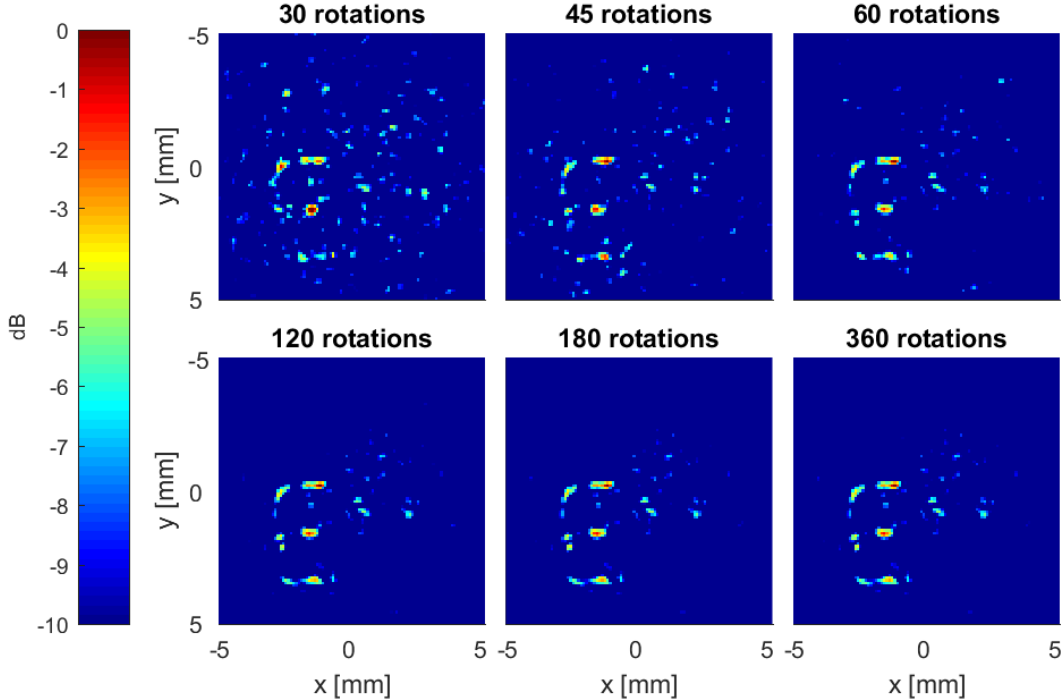

FIGURE 3.7: Reconstruction comparison for a different number of rotations.

The SNR level is approximately 5-6 dB, but some parts of the letter are better visible (horizontal stripes) than the others (vertical stripes). The reason for this is that we are performing 2D imaging of a 3D object. If the letter is slightly tilted, then some parts could be out of the imaging plane. Additionally, as the letter has width, the scatterers behind the front surface of the letter also reflect and contribute to $\mathbf{y}$.

To check this hypothesis we shifted the A-matrix by several time-samples and repeated the reconstruction (72 angles were used). Shifting all impulse-responses along the time dimension is equivalent to reconstructing another plane. Of course, this is not true 3D imaging, as, firstly - all planes should be reconstructed at once, and, secondly – we make an assumption that the wave does not change at all while propagating through such a small distance.

Figure 3.8 shows that reconstructing slightly shifted planes might accentuate other parts of the object. If that is a real 3D reconstruction, we could benefit from looking at the projection over several planes (Figure 3.9) and obtain a better estimation of the object. Several planes can be projected by summation, averaging or maximum energy principle.

Another peculiarity is that, unlike in theory, due to noise in the $\mathbf{A}$ matrix and the transducer non-uniformity (see Figure 2.13) sometimes a new equation might lead to an SNR decrease.

In this chapter the first reconstruction attempt was presented. Several practical difficulties in the process are solved by proper "cleaning" of the data and precalibration. It was shown that the number of rows in $\mathbf{A}$ can be reduced (without reducing the image quality) by a uniform choice of $\mathbf{y}$ based on the measurements' cross-correlation matrix. When subsampling the rows of $\mathbf{A}$ no relevant information is lost, because removed rows add only linearly dependent equations. This might seem as a substantial dimensionality reduction, however in reality, the number of columns (pixels) is a bigger problem and can only be tackled by spatial upsampling. It is important to understand that the correlation map is dependent on the object under investigation and the
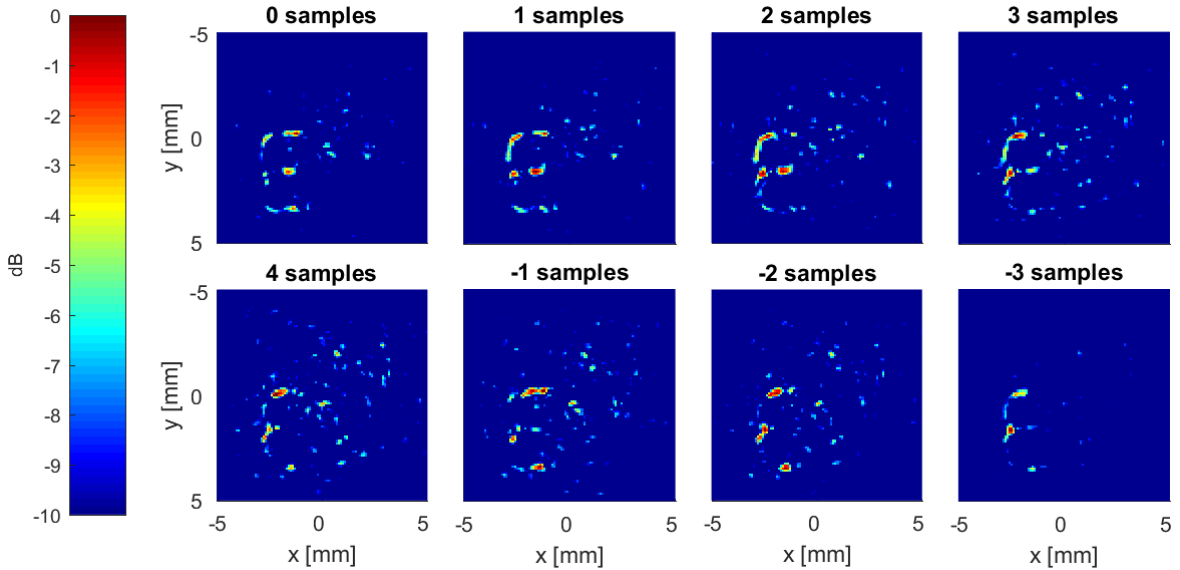
FIGURE 3.8: Reconstruction in different planes (pseudo 3D).
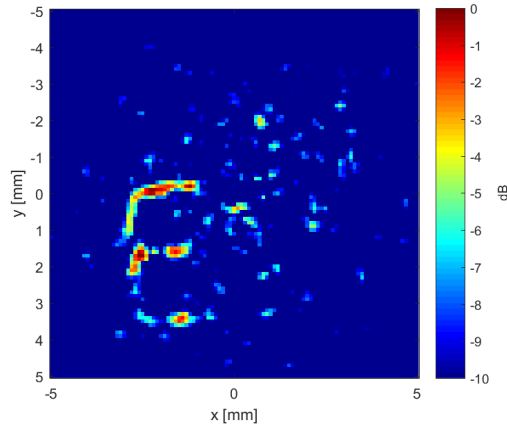
FIGURE 3.9: Projection of several reconstructions performed in shifted planes.

mask type. With more complicated masks all 360 measurements might become relevant. The adaptive non-uniform down-sampling of the rows of $\mathbf{A}$ might be a subject of future work.

The reconstruction experiment revealed that $\mathbf{A}$ integrating two spatial dimensions (as if we know the depth at which the letter is located) is not able to fully explain measurements taken from a 3D object. According to the Born approximation, after digitizing the region, every point of an object acts as an independent wave source [33, p.187]. Measurements $\mathbf{y}$ can be approximated by the summation of signals produced by all points. Even if the object or its part physically was out of the imaging plane, the algorithm treats all the data equally and will try to fit it.

By shifting the $\mathbf{A}$ matrix several samples back and forth, the simplest propagation model was implemented. This way it was indirectly confirmed that imaging a 3D region, apart from adding more unknowns, should also bring more options and better results.

Chapter 4

Constructing the A Matrix by Prediction

As was shown in Chapter 3, a straightforward measured dictionary is able to produce a good resulting image, if an object was located in the same scanning plane. This can be seen as 3D imaging with prior knowledge about one dimension. However, it is hard to position an object (which itself has three dimensions) within one sample precision not only in realistic environments, but also in the laboratory. Even if this is achieved, the reconstructed image can benefit from taking into consideration the plane right after or before the initial one.

As a result, multiple planes should be scanned. One way to do this could be – interpolating the volume between two **A**-matrices measured at different depths. However, due to the highly "random" wave field invoked by the aberration layer, interpolation gives poor results, especially later in the fast-time dimension, where the pressure field contains high spatial frequencies.

This implies that planes must be scanned at sub-wavelength distances (at least every 150 μm for a 5 MHz transducer). Scanning several planes to image an object which spans at least a couple of millimeters in depth is tedious, and also critically affects experiment duration, amount of data saved and attractiveness of the "single element imaging" idea in general.

In order to avoid that, we propose a hybrid **A**-matrix which is constructed by measurements, but just partially.

4.1 Pressure Field Prediction

4.1.1 Angular Spectrum Approach

The angular spectrum approach (ASA) is a mathematical technique for radio-wave propagation. Although there are several extensions of this method in application to ultrasound [34–36], our application is relatively simple as the medium is assumed to be homogeneous, linear and isotropic.

First, we define a source field generated by a pulsed excitation as $P_0(x, y, z_0, t)$ – a 4D matrix with three spatial dimensions (z_0 fixed) and one temporal. ASA uses knowledge of the source plane to model pressure distribution at an arbitrary parallel plane in three steps [37, 38]:

- decompose initial pressure distribution into the angular spectrum by calculating its FT;
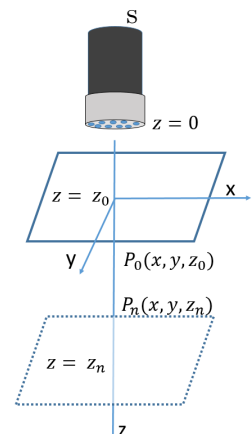- propagate every decomposed plane wave in the spatial frequency domain;

FIGURE 4.1: ASA for the wave propagation.

- superimpose propagated spectrum by the inverse FT.

The angular spectrum in the initial z_0 plane is given by the 3D Fourier transform of $P_0(x, y, z_0, t)$:

$$\hat{P}_0(k_x, k_y, z_0, f) = \iiint P_0(x, y, z_0, t)e^{-j(k_x x + k_y y + 2\pi f t)}dtdxdy, \qquad (4.1)$$

where k_x and k_y are the wave numbers along the corresponding axes. Expression (4.1) can also be called spatial frequency spectrum, because $k_x = 2\pi f_x$ and $k_y = 2\pi f_y$, where f_x and f_y are the spatial frequencies.

Similarly, the Fourier decomposition of the pressure field in the target plane z_n is given by:

$$\hat{P}_n(k_x, k_y, z_n, f) = \iiint P_n(x, y, z_n, t)e^{-j(k_x x + k_y y + 2\pi f t)}dtdxdy. \qquad (4.2)$$

The next step is propagation of the angular spectrum $\hat{P}_0(k_x, k_y, z_0, f)$ from initial plane z_0 to the destination plane z_n. This requires solving the wave equation given in (1.1):

$$\nabla^2 p - \frac{1}{c^2}\frac{\partial^2 p}{\partial t^2} = 0$$

.

After substituting p by a spatio-temporal function $p(x, y, z_0, t) \triangleq P(x, y, z_0)T(t)$ where the temporal and spatial behavior have been decoupled, the homogeneous wave equation is reduced to the Helmholtz equation [39] of the monochromatic plane wave (applying the temporal FT in (4.1) ($t \leftrightarrow f$) all frequency components are separated and forward propagation can be performed for each one).

The final solution yields that the Fourier spectrum $\hat{P}_0(k_x, k_y, z_0, f)$ evolves along the z-axis as

$$\hat{P}_n(k_x, k_y, z_n, f) = \hat{P}_0(k_x, k_y, z_0, f)e^{\pm jk_z(z_n - z_0)}, \qquad (4.3)$$

where $k_z = \sqrt{k^2 - k_x^2 - k_y^2}$ with $k = \frac{2\pi f}{c}$ the frequency dependent wave number and the $\pm$ sign in the exponential *spectral propagating factor* denotes forward or backward propagation accordingly. The solution basically states that propagation between z_n and z_0 is calculated by applying phase shifts to every component of the angular spectrum. These shifts are variable because waves have traveled different distances based on their initial angles.

The final step is to return back to the temporal domain and superimpose all harmonics into one complex wave again. Inverse 3D FT is applied to the propagated plane waves:

$$P_n(x, y, z_n, t) = \iiint \hat{P}_n(k_x, k_y, z_n, f)e^{j(k_x x + k_y y \pm k_z(z_n - z_0))}dfdk_xdk_y \qquad (4.4)$$

Comparing this approach with the one used by N.Etaix (Section 1.2.3) it can be showed that the Rayleigh-Sommerfield integral and ASA yield identical predictions of propagated fields [40]. The difference is that the spatial propagator $\dfrac{e^{-jk|\boldsymbol{r} - \boldsymbol{r}_s|}}{2\pi |\boldsymbol{r} - \boldsymbol{r}_s|}$ used in (1.7) is applied to every point, whereas ASA with the spectral propagator allows much faster computations.

Many evaluations of ASA have been done [41–43], in general showing small prediction errors. We also conduct a feasibility check before applying the ASA in our project (Section 4.1.3).

4.1.2 Hydrophone Signal Conversion to Pulse-echo

ASA works with pressure fields measured at a plane in space, which implies collecting data with a hydrophone. Also, the output of the ASA is a forward propagated pressure. At the same time we need to fill the **A**-matrix with pulse-echoes to match measurements **y** done by the transducer. In order to account for imaging settings we refer to the *reciprocity theorem* [44]. It tells us that if $h_{\mathbf{s},\mathbf{r}}(t)$ is the propagation impulse response from the source **s**, recorded at the receiver point **r**, then $h_{\mathbf{s},\mathbf{r}}(t) = h_{\mathbf{r},\mathbf{s}}(t)$ – source and receiver are interchangeable. Indeed, the hydrophone-recorded signal $h_{\mathbf{s},\mathbf{r}}$ contains all propagation effects exactly at half-way of pulse-echo distance. If we send the impulse response again in the opposite direction, the transducer will receive the convolution of the excitation signal with the channel transfer function – $h_{\mathbf{s},\mathbf{r}} * h_{\mathbf{r},\mathbf{s}}$. Assuming reciprocity, this received signal is the auto-convolution $h_{\mathbf{s},\mathbf{r}} * h_{\mathbf{s},\mathbf{r}}$ of the impulse response. We corroborate this hypothesis in practice in the following sections.

4.1.3 Feasibility Check

Before switching to a new approach, we check the validity of the ASA. To do so, the pressure field at four different planes, was measured. The first one was located close to the source and acted as ASA input (source plane). The other three were located at 1, 5 and 10 mm from the source plane (Figure 4.2) and were used as reference. In addition, pulse-echo signals were measured at the same locations. Our goal was to estimate the back-propagated RF signals when only the pressure at the source plane is known, and compare the result with the references. We also wanted to evaluate if the prediction is more accurate when planes closer to he source plane are considered.

Our modeling method is separated into two steps, namely, forward propagation using ASA and back-propagation made by the auto-convolution. We will consider each step separately to see which one is more prone to errors and offers better stability.

Figure 4.3 shows a comparison between experimentally measured and simulated forward fields at 1 mm from the source plane. Figure 4.3a compares samples in the beginning of the signal (top row) with samples in the tail (bottom row), where higher frequencies are present. Figure 4.3b compares individual signals from pixels located at [0; 0] mm and [3; 3] mm.

FIGURE 4.2: Ultrasound source and four parallel planes.

Figure 4.4 examines pulse-echo similarity between experimental and simulated fields. The latter results from the auto-convolution of what is shown in Figure 4.3. The former is measured by placing a point scatterer at the same locations, where previously the hydrophone was. Notice that echoes extend further in time than hydrophone signals.

With these results we observe that the ASA theory holds in practice – the simulated forward field in high degree replicates the experimental data. Going a step further, observing the back-propagated signals, the misfit is larger, especially in the tail of the echo. Of course, if a small error is present in the forward field model, the convolution process will produce more noticeable artifacts in the data. Furthermore, we should not forget that the reference data in this feasibility study does contain noise too. Similar observations are made with respect to the estimations at farther distances (5 and 10 mm from the source plane). Corresponding figures

are given in the [Appendix](#).
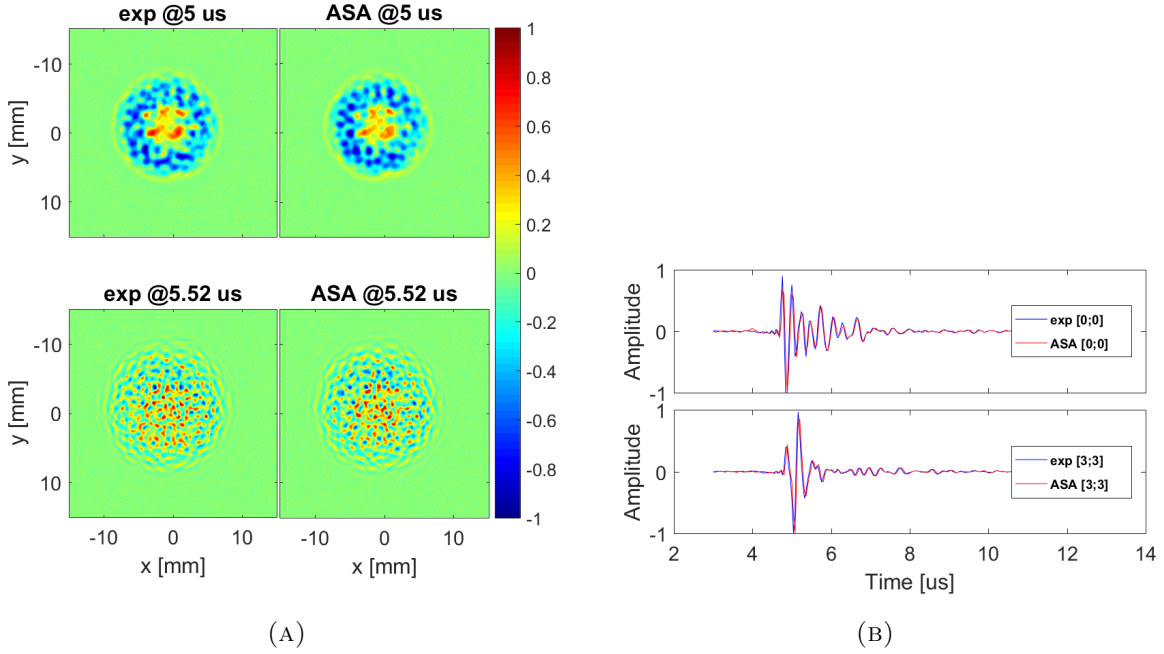
FIGURE 4.3: (A) Forward field @1mm from the source plane: measured (left) and ASA predicted (right). (B) Signal examples from two pixels: measured(blue) and ASA predicted (red).
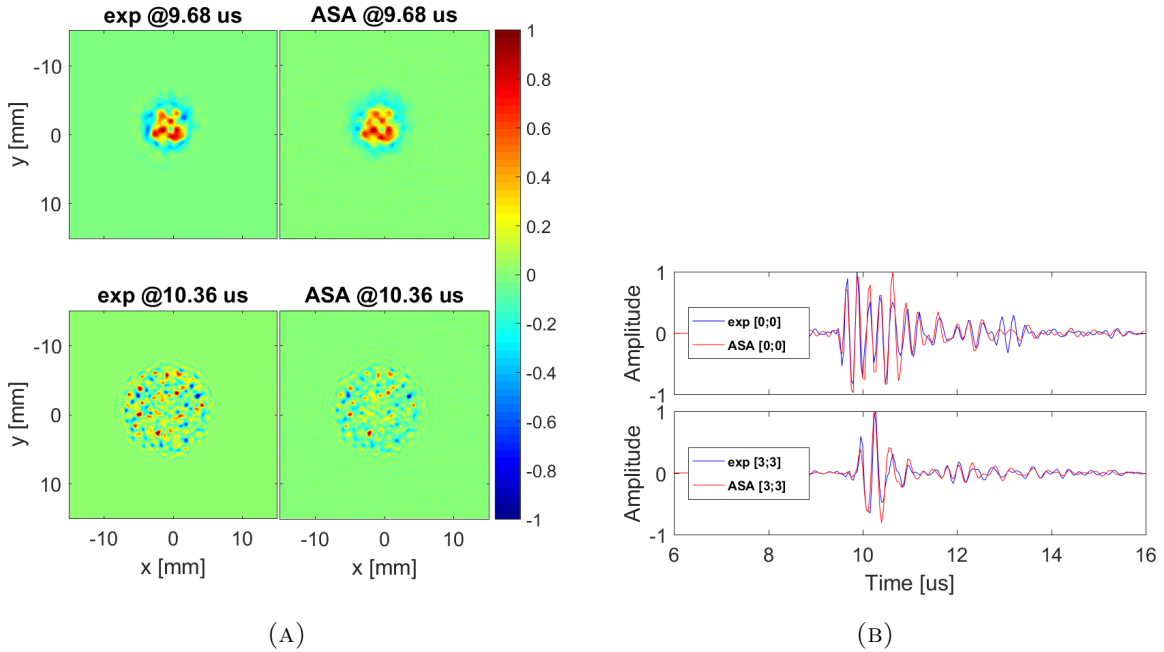
FIGURE 4.4: (A) Pulse-echo reflected @1mm from the source plane: measured (left) and ASA predicted (right). (B) Signal examples from two pixels: measured(blue) and ASA predicted (red).

Figure 4.5 presents error maps – the root mean square (RMS) error for every pixel in the entire planes at distances 1 mm (4.5a) and 5 mm (4.5b). The RMS is calculated using the experimental data EXP as a reference:

$$e_{RMS} = \sqrt{\frac{\sum(ASA - EXP)^2}{\sum EXP^2}} \tag{4.5}$$

Predicted and measured (reference) time signals are compared sample-by-sample, errors are squared and summed. The resulting value is scaled by the reference signal energy. In general, the proposed simulation algorithm produces a small error of 3%, which is not highly dependent on the pixel location and, what is more important, the quality of the estimation does not degrade with distance – errors for the estimated pressure fields at 1 and 5 mm are within the same range. The error maps corresponding to the 10 mm distanced plane exhibit similar behavior.

Another valuable observation – the ASA is able to estimate wave fields even if they originated from distinct locations. Remember that the pressure wave is generated at the transducer surface (first origin), but later it encounters the mask and is severely diffracted (the second origin). Even though this fact does not allow to back-propagate the source plane and recover the initial transducer excitation, the ASA significantly reduces the calibration procedure timing.
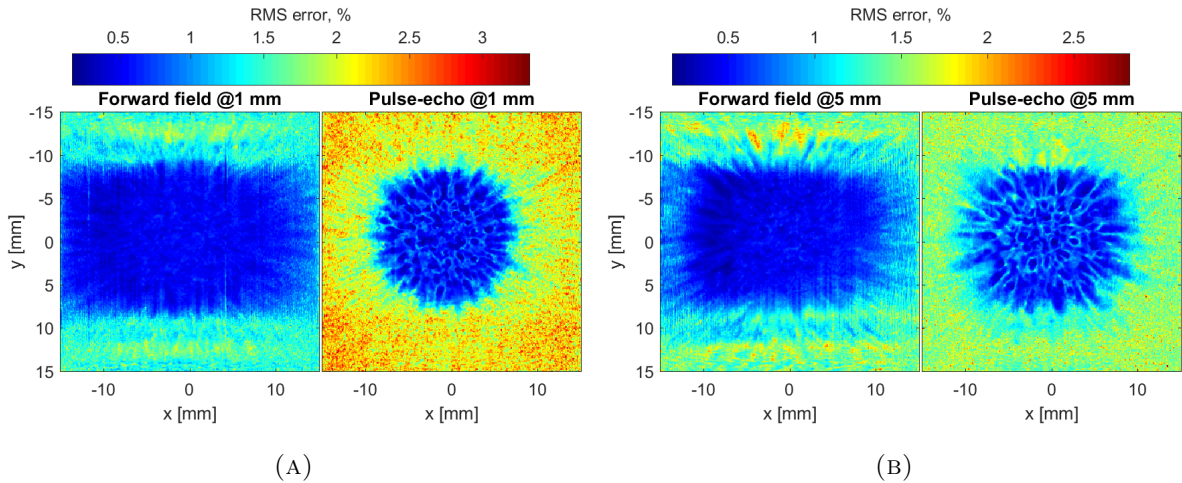
FIGURE 4.5: (A) Relative RMS error between the proposed prediction method and measurement: only forward field (left) and pulse-echo field (right) @1mm distance from the source plane. (B) Relative RMS error between the proposed prediction method and measurement: only forward field (left) and pulse-echo field (right) @5mm distance from the source plane.

4.2   Mask Effect

4.2.1   Axial Beam Profile

As shown before, the mask usage leads to significant changes in energy distribution in the plane parallel to the transducer surface. Figures 2.2 and 2.4 show the energy projection over all time samples, as for the reconstruction – every sample is treated as a separate equation. Therefore, it is worth to compare the beamprofile at sample level (Figures 4.6 and 4.7).

From these images we can conclude that the "bare" transducer's pixels in the ROI are highly spatially coherent. So, if the center pixel has a well defined peak or dip, then all other pixels are in the same phase too. The mask effectively distorts this symmetry, making this effect more apparent with time. As the slice is selected farther in time, higher frequencies appear in the beam profile. Additionally, the echo stretches slightly in time due to the fact that the emitted spherical wave is delayed non-uniformly when passing through the PMMA layer ($c_{PMMA} \approx 2 \cdot c_{water}$).

An obvious, but important notion, is that the echo variability in rotation depends on the pixel location. Pixels closer to the center have slower angular speed as shown in Figure 4.8. Ultimately, the center point (axis of rotation) does not change regardless of the mask position.
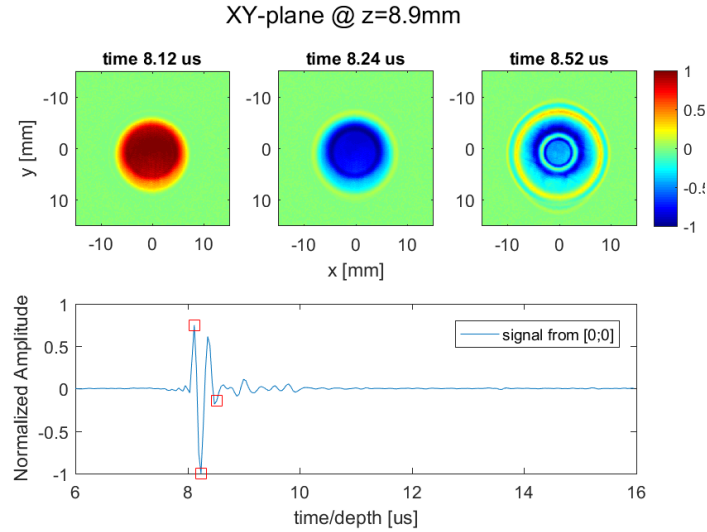
FIGURE 4.6: Top: energy beamprofile of the transducer **without the mask** for three samples (normalized). Samples at which slicing was made are shown with red markers. Bottom: signal corresponding to the center point of the ROI
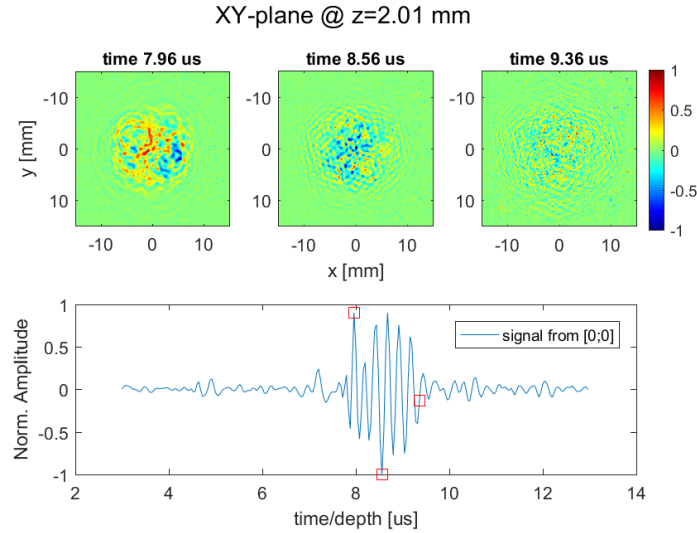
FIGURE 4.7: Top: beamprofile of the transducer **with the mask** for three samples (normalized). Samples at which slicing was made are shown with red markers. Bottom: hydrophone signal corresponding to the center point of the ROI

4.2.2 Lateral Beam Profile

The mask should be made from a material with acoustic properties that differ substantially from the ones of the medium. This will ensure larger phase shifts and more interference in the field. Previously, only the speed of sound was mentioned, however the attenuation coefficient will change in most cases. This situation directly affects the penetration depth of the beam. The beam profile along the lateral direction (Figure 4.9) confirms this consideration: due to the PMMA layer, the beam becomes more dissipated, the directivity pattern changes and also the beam's amplitude fades faster in depth. According to the energy decay, it is advisable to perform imaging at depth < 3 cm. This does not represent a problem in practice – this depth is enough, for instance, to image a carotid artery in vivo. For comparison, other mask beam profiles are provided in the Appendix.
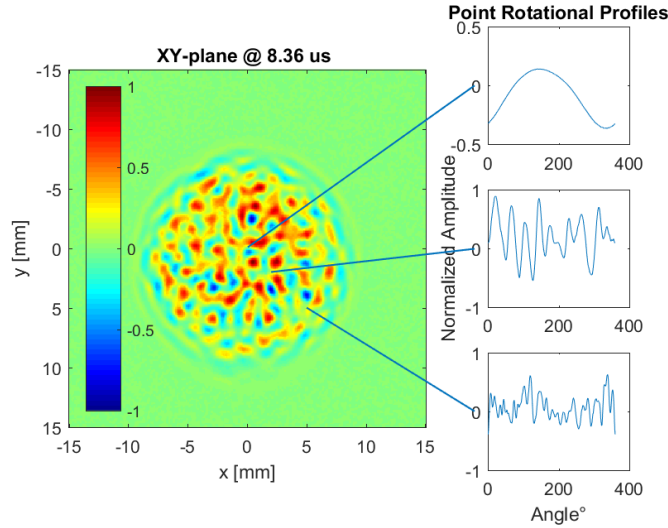
FIGURE 4.8: Point rotational variance dependence on pixel location.
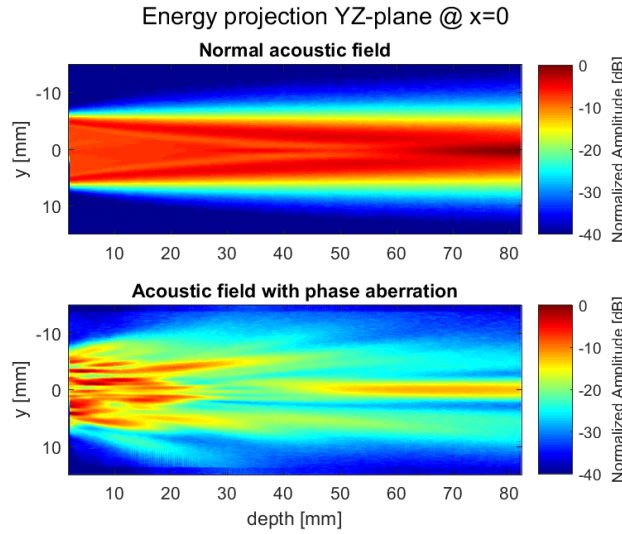
FIGURE 4.9: Comparison of in-depth beam profiles with (bottom) and without (top) the mask. Vertical axis are aligned with the transducer surface, horizontal axis is depth in mm.

4.3   3D imaging

Similarly as in Chapter 3, we image a letter using the proposed hybrid **A**-matrix, but this time truly in 3D. Employing the ASA allows us to acquire a single plane scan and predict the pressure as far in depth as needed. Assuming that the problem with the 2D imaging was that information contained in **y** is not found in **A** unless the full volume is covered. We hope to produce better images using a full 3D approach.

It is important to scan a large enough source plane containing most of the emitted energy. After acquiring information from the source plane, the "E" letter was placed in the water-tank and measurements of **y** obtained. This time we do not know where the letter is (the location is different from the scanned surface). Limited memory resources do not allow us to keep in RAM and process many planes simultaneously. In order to overcome the problem, we estimate the approximate distance to the letter from the acquired **y** and c_{water} = 1491 m/s – 1.5 mm. Shortened experiment description is given in Algorithm 1. Notice that the first two procedures are done only once and afterwards the data is used for reconstruction.

Algorithm 1 Experiment Description

```
Measure hydrophone pressure in the source plane slice₀
Measure the ringing signal in empty space (without a scattering object)
for d=1:n:360 do
   Measure pulse-echo response from an object for every mask rotation
end for
for s = 1 : N_slices do
   Predict pressure plane slice_s
   Convert forward field slice_s ⟶ pulse-echo A_s
   for d = 1 : n : 360 do
      Rearrange A_s columns according to a rotation degree d
      Stack reformatted A_s into the final A
   end for
end for
Subtract ringing from y and solve Ax = y
```

4.3.1 Reconstruction Results

As explained in Section 2.2, we reformulated the problem according to (2.14), using Tikhonov Regularization, however the imaging problem is still solved by conjugate-gradient-based methods.

The letter width is less than a millimeter and only the surface is covered with reflective powder, hence the backside will reflect much less. Thus, we initialize the ASA algorithm with the initial prediction plane at 1.3 mm. The back-plane of the ROI is defined by two parameters – number of slices to simulate and dx – distance between them. As the letter is a continuous object, it is logical to set dz very small, down to one sample equivalent (40 ns). This would require too many planes. For comparison, we first assign $dz = 0.1$ mm and $N_{slices} = 4$ (Figure 4.10), then denser grids with $dz = 0.03$ mm (Figure 4.11a) and $dz = 0.02$ mm (Figure 4.12a) are used, increasing the number of planes accordingly.
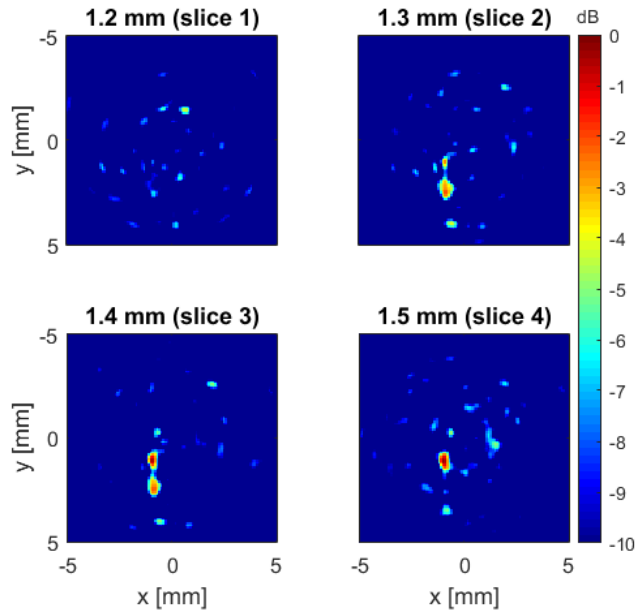
FIGURE 4.10: LSQR reconstruction with $dz = 0.1$ mm, 4 slices, size(A) = 18120×40000, $\kappa(A) = .835e^9$ (10 dB range).

When the dz grid is relatively coarse (Figure 4.10), some of the letter features are not seen at all – the algorithm tries to "explain" **y** only with available columns of **A**. When more densely located planes are imaged, other parts of the letter appear.

FIGURE 4.11: (A) LSQR reconstruction with $dz = 0.03$ mm, 6 slices,
size(A) $= 18120 \times 60000$, $\kappa(A) = 72e^9$ (10 dB range).
(B) 2D projection over all slices.

FIGURE 4.12: (A) LSQR reconstruction with $dz = 0.02$ mm, 8 slices,
size(A) $= 18120 \times 80000$, $\kappa(A) \gg 72e^9$ (10 dB range).
(B) 2D projection over all slices.

In this case, the **A** matrix is severely underdetermined – the number of unknowns is increasing substantially with adding just one extra plane, but the number of equations is fixed after the number of angles to be used has been fixed. Exploiting the knowledge from the 2D imaging case, we use 120 **y**'s (each 150 samples long).

The condition number is extremely large, because of the ROI dimensions and it grows linearly with more slices. As we are imaging a very thin volume (lateral≫axial dimension), many of the columns of **A** look like slightly shifted versions of each other, which leads to collinearity phenomena. In fact, it is not even necessary to estimate so closely located slices as simple shifting in time provides perfect prediction. As a result, we only need to employ the ASA to propagate the field to the initial depth in which we want to start imaging.

The images also show the letter projection as if we look at it in XY-plane. As more planes are projected, reconstruction quality increases and the noise level becomes lower.

To illustrate that we do not compromise the quality of the results when using the iterative scheme together with Tikhonov regularization, without precomputing the SVD, we also provide the result of traditional Tikhonov reconstruction (solving the normal equations) for the case of

$dz = 0.03$ mm (Figure 4.13a). Comparing with Figure 4.11a, noise is reduced slightly, a better image can not be retrieved from the same data.
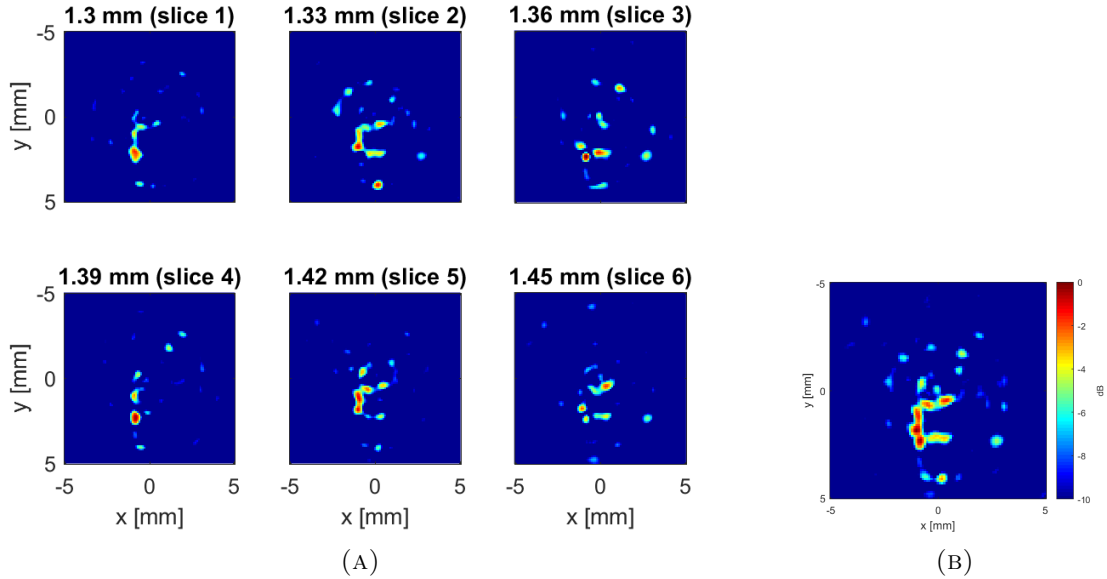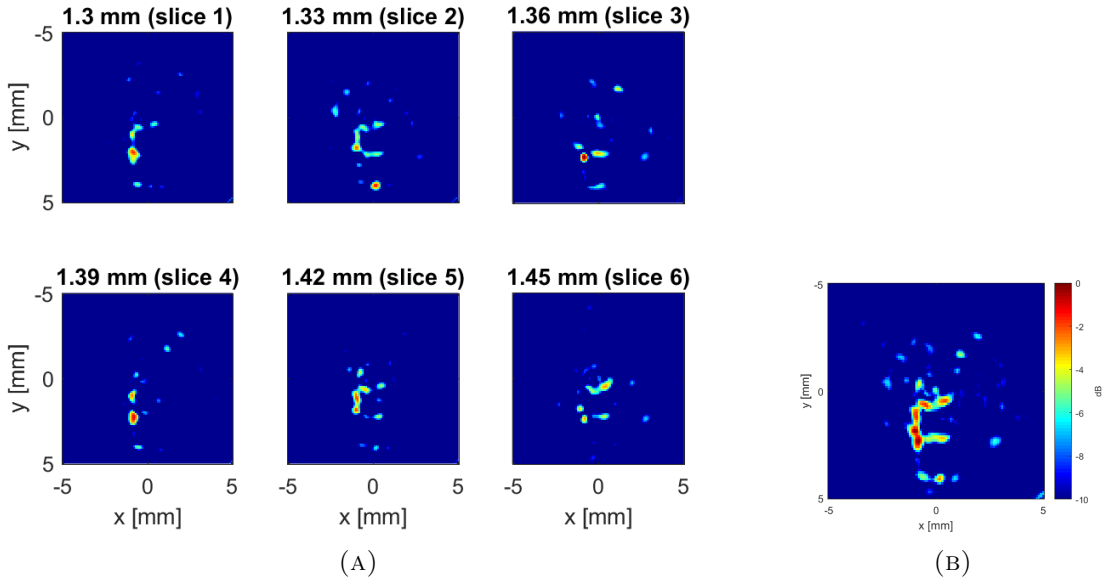

FIGURE 4.13: (A) Tikhonov reconstruction with $dz = 0.03$ mm, 6 slices,
size(A) = 18120×60000, $\kappa(A) = 72e^9$ (10 dB range).
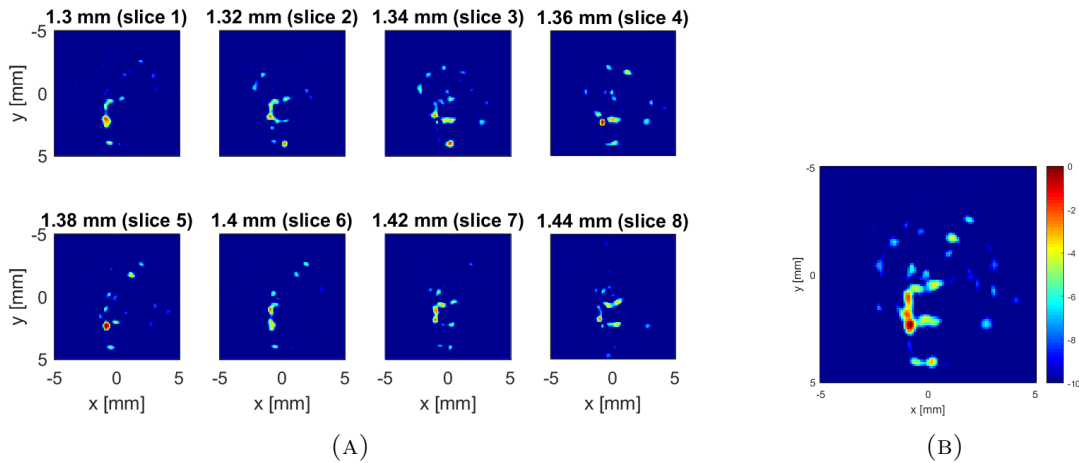(B) 2D projection over all slices.

4.3.2 l_1 Reconstruction

The problem as it is stated in (2.10) is an l_2 optimization problem. While Tikhonov regularization is relevant for numerical stabilization of the solution, we still observe many active pixels which are not part of the object (low SNR). The solution provided by l_2 methods, in general, limits the coefficient values, but many of them still remain non-zero. Moreover, if λ is chosen large, the solution of the l_2 norm problem is minimized by assigning similar values to more coefficients.

Instead of shrinking the coefficients, l_1 regularization aims to search for a solution in which most of the coefficients are zero, in other words it induces *sparsity* in the estimate. It can be said that in our experiment the spatial variation of the speed of sound is measured and presented as color intensity values. Hence, the sparsity assumption is valid in the spatial domain, because the letter covers only part of the water-filled volume.

The Lagrange form of the l_1 regularized problem (also called LASSO [45]) becomes

$$\underset{x}{\text{minimize}} \ \|\mathbf{A}\mathbf{x} - \mathbf{y}\|_2^2 + \lambda\|\mathbf{x}\|_1, \tag{4.6}$$

where again λ is a parameter used to weight the two penalties.

The same data as previously was supplied to the LASSO solver. The practical difference between l_2 and l_1-based solutions can be seen immediately (Figure 4.14). In the latter case the object trace is much more compact or simply sparse. It is too "costly" for the minimization problem to light up active pixels close to one another. The algorithm assigns higher brightness values to several distinct points and makes the neighbors 0. As a result, the reconstruction fits into one plane instead of being spread over larger depth (this potentially leads to a smaller $\mathbf{A}$ matrix). Also, in the l_1 case there is no trend to make coefficients equal, hence higher dynamic range is needed to see the letter.
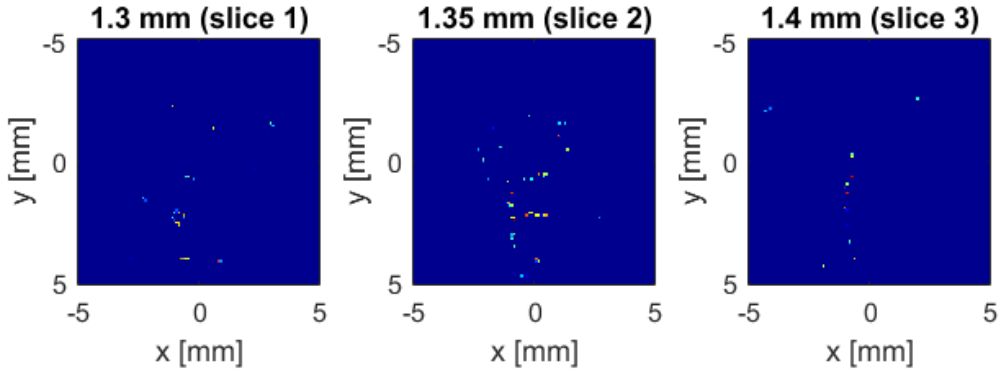
FIGURE 4.14: Letter reconstruction with $dz = 0.05$ mm and l_1 algorithm (30 dB range)

4.3.3 Lateral Resolution

Lateral resolution is the ability to resolve objects perpendicular to the beam axis. Another experiment was conducted to see at what separation distance two laterally separated points can still be resolved. For this purpose we imaged two single point scatterers that where positioned at equal depth. One was set at a fixed position and the other one was moved along the x-axis. Reconstructed images are given at Figure 4.15. According to that, lateral resolution is $\approx 0.6 - 0.7$ mm or 2λ ($\lambda = 0.3$ mm).
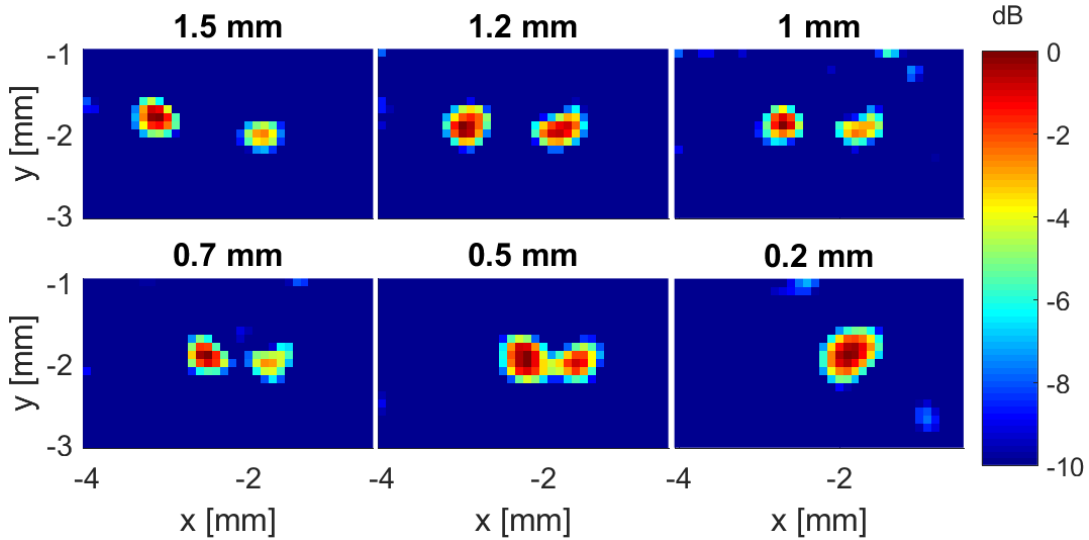
FIGURE 4.15: Defining lateral resolution based on two point scatterers reconstruction.

Lateral resolution can be improved by using the transducer with larger aperture or higher f_0. From the computational point of view, the aberration layer producing more diverse and longer echoes is expected to enhance resolution.

Assuming a specific application (where it is known in advance that a volume contains a few distinct scatterers), l_1 algorithms are able to reach resolutions as small as the pixel size.

4.3.4 Imaging through a Tissue-mimicking Phantom

An important question accompanying every concept is its real-life usage. Previously shown results prove that after calibration has been done in homogeneous media (water), imaging is successful in the same environment. Assuming an in-vivo application for our method, the ultrasound waves will imminently encounter several layers with various acoustic properties (skin, tissue, etc.). The calibration procedure (involving pressure field measurements) every time before imaging, would make the approach unpractical. To observe how the presence of additional inhomogeneity would affect the data, the following experiment was conducted.
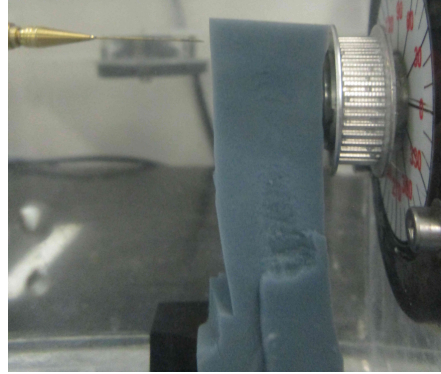
FIGURE 4.16: Imaging through a tissue-mimicking phantom.

Firstly, we recorded one plane of acoustic pressure data the same way as it was done throughout this thesis. Then we positioned a 1 cm thick piece of a *tissue-mimicking material* (TMM) between the imager and the hydrophone (Figure 4.16). The realistic tissue-mimicking phantom was made according to the recipe of Teirlinck *et al.* [46]. The speed of sound $c_{TMM} = 1551$ m/sec.

Figure 4.17 compares the acquired RF signals. Due to the attenuation made by the TMM, we normalized the pressure to the [-1;1] range to invalidate amplitude changes. Furthermore, a phase shift of two samples is applied in order to obtain a correct comparison. This shift appears due to a small difference between speed of sound in water and in the TMM.
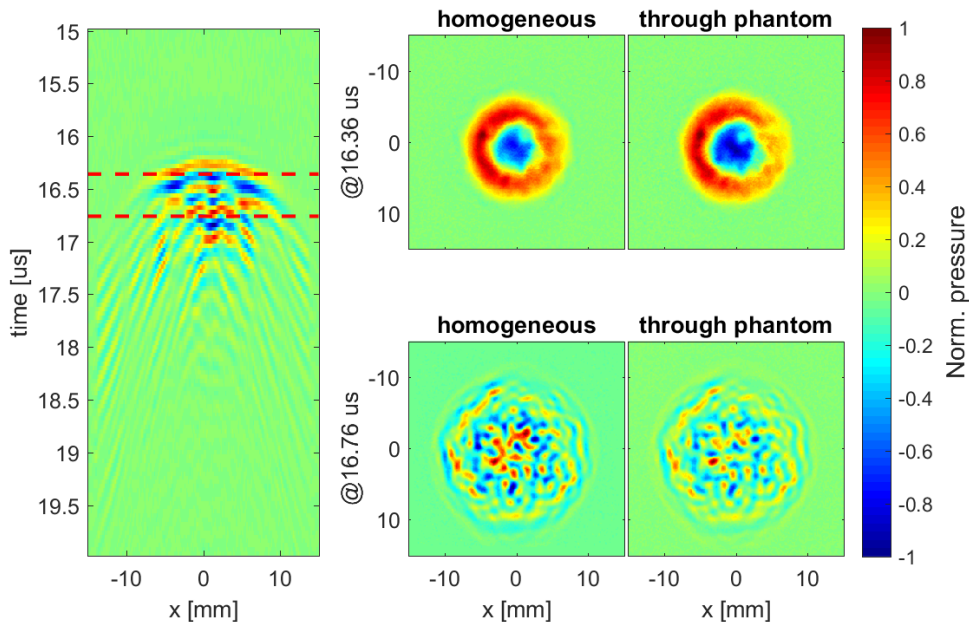
FIGURE 4.17: Imaging through tissue-mimicking phantom. The left pane: slice through a 3D RF matrix. The right pane: sample-by-sample comparison of signals measured with (right) and without (left) TMM.

The results show some discrepancies in the beam profiles, mostly due to higher spatial spreading. These changes are not negligible, but, in overall, we think the presence of a relatively thin skin layer should not ruin the reconstruction.

Discussion and Conclusions

Low-cost hardware is a highly desired goal in various 3D imaging applications. We have proposed a possible solution to this problem in the ultrasound domain. It was shown that an arbitrary scattering layer between a single element transducer and an object leads to naturally multiplexed measurements. Inheriting some insights from the compressive sensing field and earlier works on time reversal theory, this thesis has shown that an image can be reconstructed only by knowing the transducer's spatial field.

One of the major challenges is to obtain a precise pressure distribution after the wave-mask collision. A calibration procedure, used to capture temporal traces at every spatial point, was described in detail. Although, it needs to be done only once, we have significantly reduced the timing by employing the angular spectrum approach for the pressure field modeling. It was experimentally proved that our ASA implementation for pulsed broadband ultrasound waves provides very good prediction results, independently of the mask design or prediction depth.

Another inevitable problem is an effective algorithm able to solve large-scale least squares problems. In order to become amenable for real-time applications, orders of magnitude improvements in processing time is required. Reconstruction timing is in the range of minutes even for the simplest problems. In order to solve 3D problems with many thousands of unknowns we employed an lsqr-type iterative procedure combined with Tikhonov regularization. SVD-based reconstruction performed on a powerful computer showed little enhancement. Also if the signatures of close pixels are almost coherent the dictionary is not suitable for sparse reconstruction.

Optimal mask design is the key to finer resolution, better system conditioning and higher SNR. In this work, we provided a comparison of several static mask designs. The SVD decomposition of a system matrix $\mathbf{A}$ and measurements' cross-correlation matrix are proposed as the mask evaluation parameters. For a good final image, the mask has to result in many phase shifts and spatial diversity in the transducer's beam profile. The mask rotation is proposed as one way to collect more compressed data without altering the framework.

In the end, we were able to perform real 3D reconstruction of a plastic letter in water. Given examples showed that balance has to be found between the number of imaging planes, grid size and data samples. Approximate lateral resolution is in the range of 2λ, which is impressive considering the number of sensors. The homogeneity assumption, of course, does not hold in real life, but we have shown that a layer of tissue-like material does not seriously affect a prerecorded $\mathbf{A}$. A bigger issue with in-vivo measurements would be a time-varying media for which the $\mathbf{A}$ should be adapted.

Some deviation from the extreme case we followed would help increasing quality of images and make the approach more practically realizable. For example, making a few elements transducer would not boost the price a lot, but significantly help with the conditioning of the problem. Another way is to add more advanced technologies to the mask – temperature/frequency dependence and material combination. Might be that a proper combination of a wave-diffusing mechanism and a small linear probe could eliminate the need for rotation.

As stated in the very beginning, a big advantage of ultrasound diagnostics is its real-time control. In our case one tiny image takes minutes to show on a screen. Although, some of the procedures described in this thesis can be done in advance (precalibration), it would be useful to parallelize the reconstruction.

On the whole, to be considered for real clinical usage, more work has to be done on tasks such as:

- Acoustic wave 3D simulations in non-homogeneous, but well characterized media with high precision and in realistic time;
- New insights in solving badly conditioned linear systems with application to ultrasound-specific tasks;
- Methods and technologies to promote ultimate spatial diversity of a propagating wave.

Nevertheless, we believe that the work described in this thesis might be the first step to "computational ultrasound" – affordable and easy-to-use imagers, another example of body area sensors so popular nowadays in medicine, sports and consumer electronics.

Bibliography

[1] K. Kirk Shung and Michael J. Zipparo. Ultrasonic transducers and arrays, 1996. ISSN 07395175.

[2] Richard Baraniuk, Mark a Davenport, Marco F Duarte, and Chinmay Hegde. An Introduction to Compressive Sensing. *Connexions, Rice University, Houston,Texas*, page 118, 2011. URL http://cnx.org/content/col11133/1.5/.

[3] Dr. Joseph Woo. A short History of the development of Ultrasound in Obstetrics and Gynecology, 2015. URL http://www.ob-ultrasound.net/history1.html.

[4] Jacques Curie and Pierre Curie. Développement, par pression, de l'électricité polaire dans les cristaux hémièdres à faces inclinées. *Comptes-Rendus de l'Académie des Sciences*, 91: 294–295, 1880.

[5] Thomas Szabo. *Diagnostic ultrasound imaging: inside out*. Elsevier Inc., 2004. ISBN 0126801452.

[6] H Azhari. *Basics of Biomedical Ultrasounds for Engineers*. Wiley-IEEE Press, 2010. ISBN 9780470465479.

[7] K. Kirk Shung. Ultrasonic Scattering in Biological Tissues, 1993. ISSN 00014966.

[8] Sarah B. Murthi, Mary Ferguson, and Amy C. Sisley. *Diagnostic Ultrasound Physics and Equipment*. Cambridge University Press, 2nd edition, 2010. ISBN 9780387798295. doi: 10.1007/978-0-387-79830-1_4. URL http://link.springer.com/10.1007/978-0-387-79830-1{_}4.

[9] Julien Richy. *Compressive Sensing in Medical Ultrasonography*. PhD thesis, Kungliga Tekniska Högskolan, 2012. URL http://kth.diva-portal.org/smash/get/diva2:538788/FULLTEXT01.pdf.

[10] Jorgen Grythe and Norsonic As. Beamforming algorithms - beamformers, 2015.

[11] K.E. Thomenius. Evolution of ultrasound beamformers. *1996 IEEE Ultrasonics Symposium. Proceedings*, 2:1615–1622, 1996. ISSN 1051-0117. doi: 10.1109/ULTSYM.1996.584398.

[12] Murtaza Ali, Dave Magee, and Udayan Dasgupta. Signal processing overview of ultrasound systems for medical imaging, 2008. URL http://cdn.medicexchange.com/images/whitepaper/signal-processing-overview-of-ultrasound-systems.pdf.

[13] RCEMLearning. Ultrasound: Physics and Basic Equipment Settings, 2015. URL http://www.rcemlearning.co.uk/modules/ultrasound-physics-and-basic-equipment-settings/types-of-ultrasound/amode/.

[14] Claude E. Shannon. Communication in the Presence of Noise. *Proceedings of the IRE*, 37 (1):10–21, 1949. ISSN 00968390. doi: 10.1109/JRPROC.1949.232969.

[15] Dharmpal Takhar, Jason N Laska, Michael B Wakin, Marco F Duarte, Dror Baron, Shriram Sarvotham, Kevin F Kelly, and Richard G Baraniuk. A new compressive imaging camera architecture using optical-domain compression. *Procedures of Computational Imaging*, 6065:606509–606509–10, 2006. ISSN 0277786X. doi: doi:10.1117/12.659602.

[16] Antoine Liutkus, David Martina, Sébastien Popoff, Gilles Chardon, Ori Katz, Geoffroy Lerosey, Sylvain Gigan, Laurent Daudet, and Igor Carron. Imaging with nature: compressive imaging using a multiply scattering medium. *Scientific reports*, 4(5):5552, 2014. ISSN 2045-2322. doi: 10.1038/srep05552. URL http://www.ncbi.nlm.nih.gov/pubmed/25005695$\delimiter"026E30F$nhttp://www.pubmedcentral.nih.gov/articlerender.fcgi?artid=4087920{&}tool=pmcentrez{&}rendertype=abstract$\delimiter"026E30F$nhttp://www.nature.com/articles/srep05552.

[17] John Hunt, Tom Driscoll, Alex Mrozack, Guy Lipworth, Matthew Reynolds, David Brady, and David R Smith. Metamaterial Apertures for Computational Imaging. *Science*, 339(6117):310–313, 2013. ISSN 0036-8075. doi: 10.1126/science.1230054. URL http://www.sciencemag.org/content/339/6117/310$\delimiter"026E30F$nhttp://www.sciencemag.org/cgi/doi/10.1126/science.1230054.

[18] S. M. Popoff, G. Lerosey, R. Carminati, M. Fink, A. C. Boccara, and S. Gigan. Measuring the transmission matrix in optics: An approach to the study and control of light propagation in disordered media. *Physical Review Letters*, 104(10), 2010. ISSN 00319007. doi: 10.1103/PhysRevLett.104.100601.

[19] N Etaix, M Fink, and R K Ing. Acoustic imaging device with one transducer. *Journal of the Acoustical Society of America*, 131(5):EL395–9, 2012. ISSN 00014966. doi: 10.1121/1.3699533. URL http://www.ncbi.nlm.nih.gov/pubmed/22559458.

[20] M Fink. Time reversal of ultrasonic fields. I. Basic principles. *IEEE transactions on ultrasonics, ferroelectrics, and frequency control*, 39(5):555–566, 1992. ISSN 0885-3010. doi: 10.1109/58.156174.

[21] G H Golub and C F Van Loan. *Matrix Computations*, volume 3rd. Johns Hopkins University Press, 1996. ISBN 0801854148. URL http://books.google.com/books?id=mlOa7wPX6OYC{&}printsec=frontcover.

[22] Gilbert Strang. Linear Algebra and its applications fourth edition. *Pressure Vessel Design Manual*, page iii, 2013. ISSN 15740072. doi: 10.1016/B978-0-12-387000-1.01001-9. URL http://linkinghub.elsevier.com/retrieve/pii/B9780123870001010019.

[23] R. Penrose and J. a. Todd. A generalized inverse for matrices. *Mathematical Proceedings of the Cambridge Philosophical Society*, 51(03):406–413, 1955. ISSN 0305-0041. doi: 10.1017/S0305004100030401.

[24] Medhat A. Rakha. On the Moore-Penrose generalized inverse matrix. *Applied Mathematics and Computation*, 158(1):185–200, 2004. ISSN 00963003. doi: 10.1016/j.amc.2003.09.004.

[25] Christopher C. Paige and Michael a. Saunders. LSQR: An Algorithm for Sparse Linear Equations and Sparse Least Squares. *ACM Transactions on Mathematical Software*, 8(1):43–71, 1982. ISSN 00983500. doi: 10.1145/355984.355989. URL http://portal.acm.org/citation.cfm?doid=355984.355989.

[26] David Chin-Lung Fong and Michael Saunders. LSMR: An Iterative Algorithm for Sparse Least-Squares Problems. *SIAM Journal on Scientific Computing*, 33(5):2950–2971, 2011. ISSN 1064-8275. doi: 10.1137/10079687X. URL http://arxiv.org/abs/1006.0758.

[27] G. Golub and W. Kahan. Calculating the Singular Values and Pseudo-Inverse of a Matrix, 1965. ISSN 0887-459X.

[28] Per Christian Hansen. *Discrete Inverse Problems.* Society for Industrial and Applied Mathematics Philadelphia, Philadelphia, 2010. ISBN 978-0-89871-696-2. doi: http://dx.doi.org/10.1137/1.9780898718836. URL http://epubs.siam.org/doi/book/10.1137/1.9780898718836.

[29] Richard Aster, Brian Borchers, and Clifford Thurber. *Parameter Estimation and Inverse Problems.* Academic Press, 2013. ISBN 9780123850485. doi: 10.1016.

[30] Ivan Markovsky and Sabine Van Huffel. Overview of total least-squares methods. *Signal Processing*, 87(10):2283–2302, 2007. ISSN 01651684. doi: 10.1016/j.sigpro.2007.04.004.

[31] H.W. Persson and C.H. Hertz. Acoustic impedance matching of medical ultrasound transducers. *Ultrasonics*, 23(2):83–89, 1985. ISSN 0041624X. doi: 10.1016/0041-624X(85)90037-X. URL http://www.sciencedirect.com/science/article/pii/0041624X8590037X.

[32] Libo Wang, Lianlin Li, Yunbo Li, Hao Chi Zhang, and Tie Jun Cui. Single-shot and single-sensor high/super-resolution microwave imaging based on metasurface. *Scientific Reports*, 6(October 2015):26959, 2016. ISSN 2045-2322. doi: 10.1038/srep26959. URL http://www.nature.com/articles/srep26959.

[33] Richard S. C. Cobbold. *Foundations of Biomedical Ultrasound.* Oxford University Press, 2006. ISBN 9780199775125.

[34] Christopher J. Vecchio, Mark E. Schafer, and Peter A. Lewin. Prediction of ultrasonic field propagation through layered media using the extended angular spectrum method. *Ultrasound in Medicine and Biology*, 20(7):611–622, 1994. ISSN 03015629. doi: 10.1016/0301-5629(94)90109-0.

[35] Urvi Vyas and Douglas Christensen. Ultrasound beam simulations in inhomogeneous tissue geometries using the hybrid angular spectrum method. *IEEE Transactions on Ultrasonics, Ferroelectrics, and Frequency Control*, 59(6):1093–1100, 2012. ISSN 08853010. doi: 10.1109/TUFFC.2012.2300.

[36] André Ritter. Modified shifted angular spectrum method for numerical propagation at reduced spatial sampling rates. *Optics express*, 22(21):12949–12958, 2014. ISSN 1094-4087. doi: 10.1364/OE.22.026265.

[37] M. Pluta, M. Schubert, J. Jahny, and W. Grill. Angular spectrum approach for the computation of group and phase velocity surfaces of acoustic waves in anisotropic materials. *Ultrasonics*, 38(1):232–236, 2000. ISSN 0041624X. doi: 10.1016/S0041-624X(99)00123-7.

[38] Joseph W. Goodman. *Introduction to Fourier Optics.* McGraw-Hill, 2004. ISBN 0974707724. doi: 10.1117/1.601121.

[39] Michael P Lamoureux. The mathematics of PDEs and the wave equation. *Seismic Imaging Summer School*, 2006. URL http://www.mathtube.org/sites/default/files/lecture-notes/Lamoureux{_}Michael.pdf.

[40] George C. Sherman. Application of the Convolution Theorem to Rayleigh's Integral Formulas. *Journal of the Optical Society of America*, 57(4):546, 1967. ISSN 0030-3941. doi: 10.1364/JOSA.57.000546. URL http://www.opticsinfobase.org/abstract.cfm?URI=josa-57-4-546.

[41] Yigang Du, Henrik Jensen, and Jorgen Arendt Jensen. Investigation of an angular spectrum approach for pulsed ultrasound fields. *Ultrasonics*, 53(6):1185–1191, 2013. ISSN 0041624X. doi: 10.1016/j.ultras.2013.02.011. URL http://dx.doi.org/10.1016/j.ultras.2013.02.011.

[42] Zeng Xiaozheng and Robert J. McGough. Evaluation of the angular spectrum approach for simulations of near-field pressures. *Acoustical Society of America*, jan 2008. URL http://www.ncbi.nlm.nih.gov/pubmed/21959306http://www.pubmedcentral.nih.gov/articlerender.fcgi?artid=PMC3259195.

[43] Xiaozheng Zeng and Robert J. McGough. Evaluation of angular spectrum approach for simulations of spherically focused ultrasound phased arrays. In *2006 IEEE International Conference on Electro Information Technology*, pages 66–71, 2006. ISBN 078039593X. doi: 10.1109/EIT.2006.252164.

[44] P. M. Morse and K. Uno Ingard. Theoretical Acoustics. *American Journal of Physics*, 38 (5):666, 1970. ISSN 00029505. doi: 10.1119/1.1976432.

[45] Robert Tibshirani. Regression Selection and Shrinkage via the Lasso, 1996. ISSN 00359246. URL http://citeseer.ist.psu.edu/viewdoc/summary?doi=10.1.1.35.7574.

[46] Carolus J.P.M. Teirlinck, Robert A. Bezemer, Christian Kollmann, Jaap Lubbers, Peter R. Hoskins, Peter Fish, Knud-Erik Fredfeldt, and Ulrich G. Schaarschmidt. Development of an example flow test object and comparison of five of these test objects, constructed in various laboratories. *Ultrasonics*, 36(1-5):653–660, 1998. ISSN 0041624X. doi: 10.1016/S0041-624X(97)00150-9. URL http://www.sciencedirect.com/science/article/pii/S0041624X97001509.

Appendices

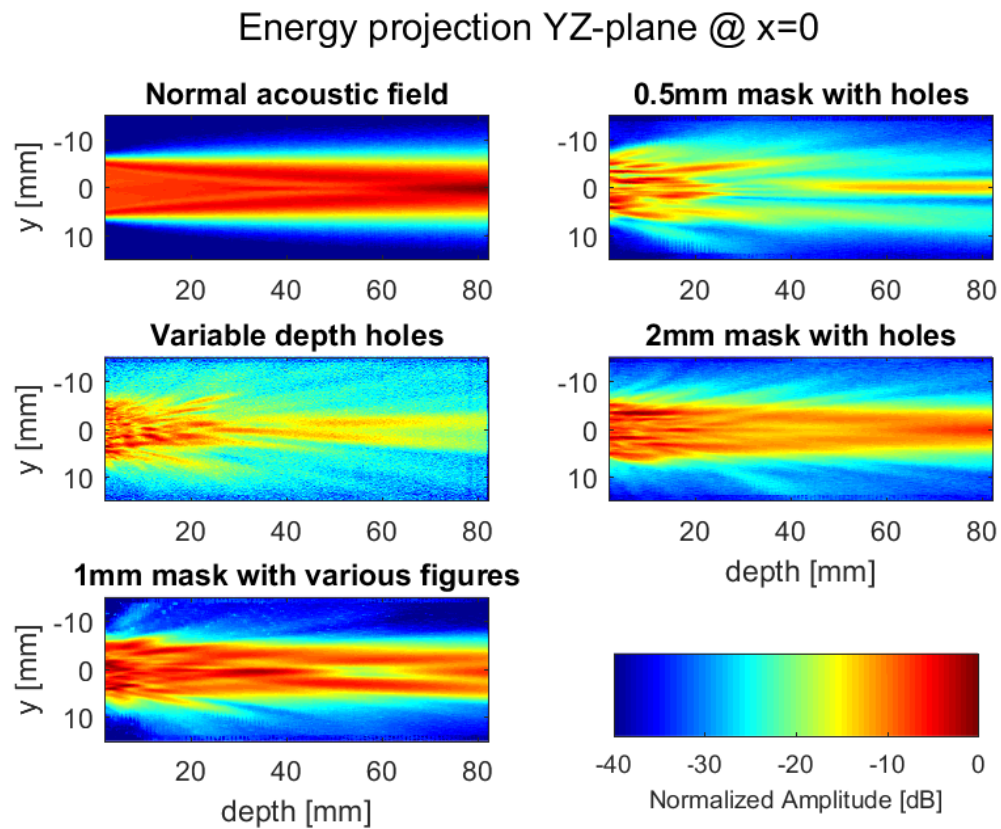# Mask Comparison - Lateral Beam Profiles

FIGURE 18: Comparison of in-depth beam profiles for different types of masks. From the top: bare transducer, the mask with variable depth surface, the mask with various shape and size holes, regular mask with holes and thickness 0.5 mm, regular mask with holes and thickness 2 mm. Vertical axis are aligned with the transducer surface, horizontal axis is depth in mm.
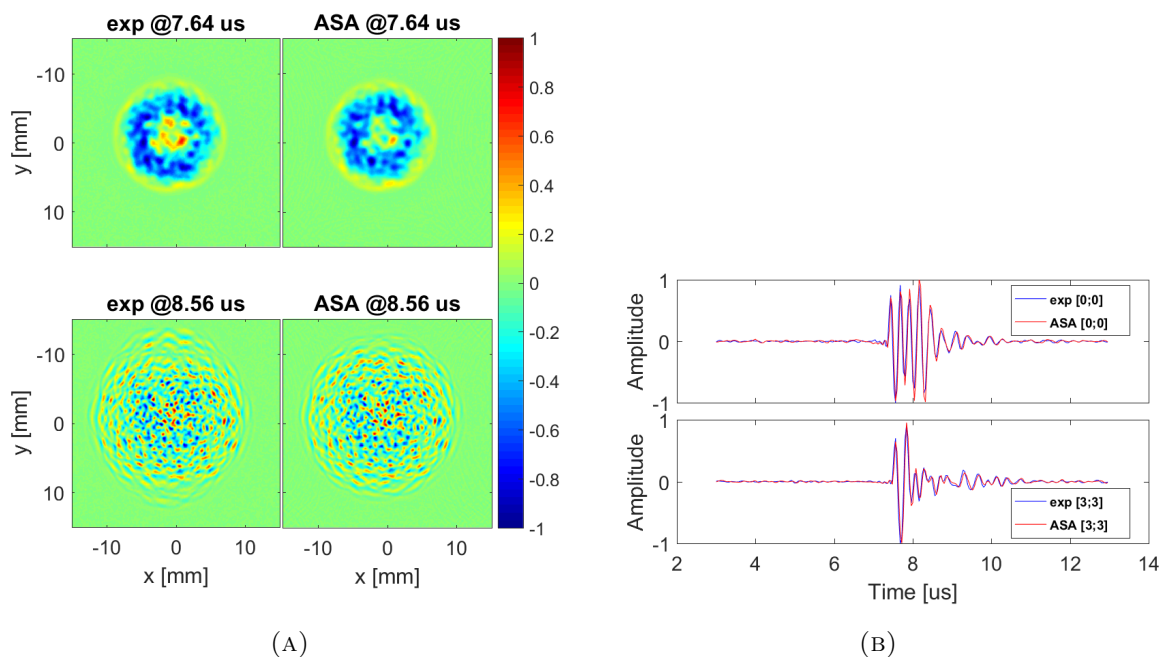
ASA Feasibility Study

(A)

(B)

FIGURE 19: (A) Forward field @5mm from the source plane: measured (left) and ASA predicted (right). (B) Signal examples from two pixels: measured(blue) and ASA predicted (red).
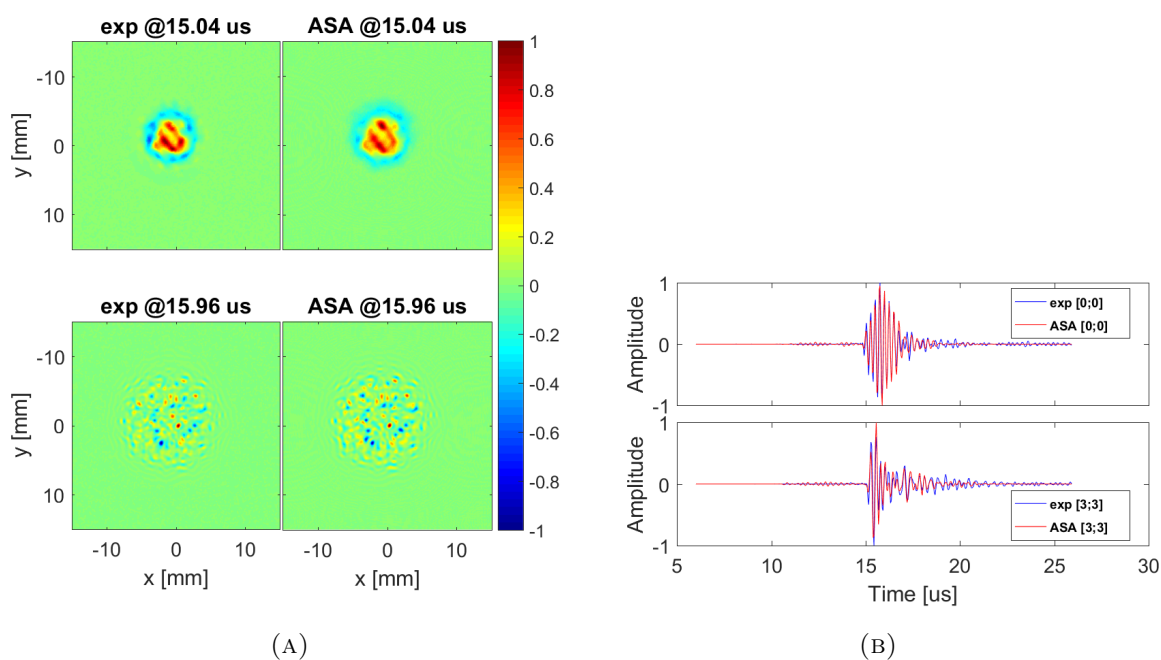

(A)

(B)

FIGURE 20: (A) Pulse-echo reflected @5mm from the source plane: measured (left) and ASA predicted (right). (B) Signal examples from two pixels: measured(blue) and ASA predicted (red).
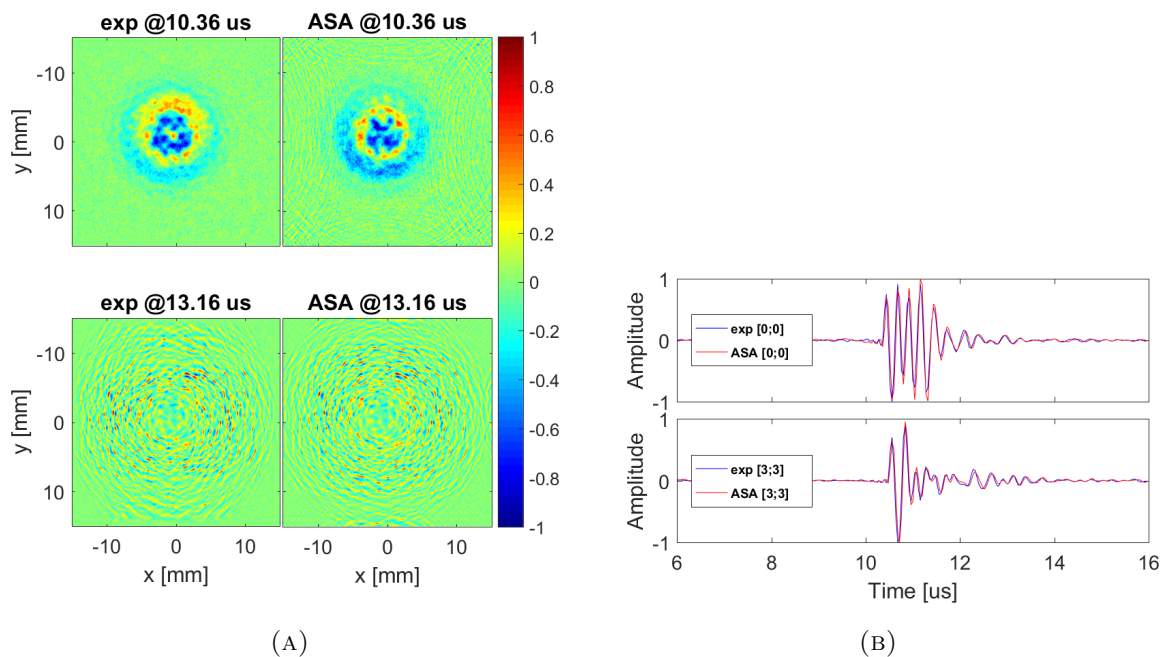
FIGURE 21: (A) Forward field @10mm from the source plane: measured (left) and ASA predicted (right). (B) Signal examples from two pixels: measured(blue) and ASA predicted (red).
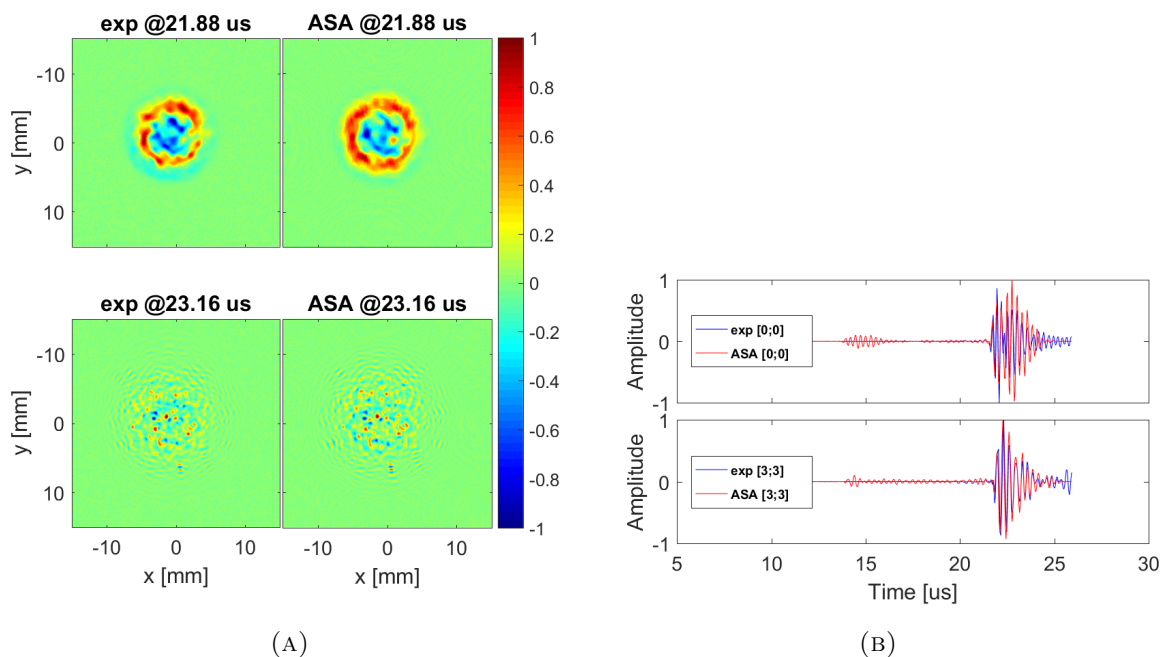

FIGURE 22: (A) Pulse-echo reflected @10mm from the source plane: measured (left) and ASA predicted (right). (B) Signal examples from two pixels: measured(blue) and ASA predicted (red).